



HAL
open science

Development of a thermo-mechanical behaviour model adapted to the ITER vacuum vessel material

Flavien Sabourin, T. Désoyer, S. Lejeunes, F. Mazerolle, V. Barabash, J.-M. Martinez

► **To cite this version:**

Flavien Sabourin, T. Désoyer, S. Lejeunes, F. Mazerolle, V. Barabash, et al.. Development of a thermo-mechanical behaviour model adapted to the ITER vacuum vessel material. *Fusion Engineering and Design*, 2021, 173, pp.112834. 10.1016/j.fusengdes.2021.112834 . hal-03326811

HAL Id: hal-03326811

<https://hal.science/hal-03326811>

Submitted on 26 Aug 2021

HAL is a multi-disciplinary open access archive for the deposit and dissemination of scientific research documents, whether they are published or not. The documents may come from teaching and research institutions in France or abroad, or from public or private research centers.

L'archive ouverte pluridisciplinaire **HAL**, est destinée au dépôt et à la diffusion de documents scientifiques de niveau recherche, publiés ou non, émanant des établissements d'enseignement et de recherche français ou étrangers, des laboratoires publics ou privés.

Development of a thermo-mechanical behaviour model adapted to the ITER Vacuum Vessel material

F. Sabourin^{a*}, T. Désoyer^b, S. Lejeunes^b, F. Mazerolle^b, V. Barabash^a, J.-M. Martinez^a

^aITER Organization, Route Vinon sur Verdon, CS 90046, 13067 St Paul lez Durance Cedex, France

^bAix Marseille University, CNRS, Centrale Marseille, LMA, Marseille, France

*Corresponding author: Flavien Sabourin, e-mail: flavien.sabourin@iter.org, Tel: +33 4 42 17 85 26

Executive summary

The ITER machine has been classified as a Basic Nuclear Installation French nuclear regulator (INB n°174), which implies that it will be the first fusion reactor to go through complete French nuclear licencing. The combination of mechanic and electromagnetic phenomena with the heat loads caused by neutron streaming requires a multi-physics approach to the damage assessment, which has not yet been implemented in the common nuclear codes and standards.

The general damage prevention methodology consists in guaranteeing the structural integrity of a component. The development of design rules has mainly two origins: prevention of damage from monotonic mechanical loads and prevention of damage from repeated application of loads. In most cases, structural integrity is justified within a linear elastic behaviour but when this route is not enough to respect the design criteria, several non-linear approaches to the material's mechanical behaviour can be considered, requiring more elaborated demonstration of the design compliance. Nevertheless, the models proposed in the nuclear model database are sometimes not sufficient to properly describe the experimentally observed cyclic plasticity behaviour and, in particular, the ratcheting and shakedown phenomena.

According to ITER community experts in materials and analyses, a thermo-mechanical behaviour model fitting the ITER Tokamak materials data will guarantee the best prediction of the damage considering a nuclear and a multi-physic loading condition.

This paper describes the assessment of the non-linear behaviour of Vacuum Vessel (VV) material with a strong thermo-mechanical coupling and a damage parameter to prevent crack initiation. More precisely, Chaboche's models available in the literature (elasto-(visco)-plasticity models, with various types of hardening) have been enriched in order to explicitly take into account the influence of the temperature on the mechanical behaviour and, reciprocally, the influence of the mechanical behaviour on the temperature. Mechanical cycling tests have been performed on the VV constitutive material, emphasizing on the progressive deformation state up to failure mode, i.e., ratcheting. The proposed models have been tested on a homogeneous problem and the results compared with uniaxial test results; this type of simulation is commonly called "0D" analysis. The last part of this document describes the finite element implementation of the constitutive material model and its application to the ITER VV welded support.

Keywords: ITER, Vacuum Vessel, thermo-mechanical coupling, material behaviour model, non-linear hardening, damage, ratcheting, SS316L(N)-IG.

1 Introduction

The ITER Organization is an intergovernmental organization based on a large scale scientific experiment that aims to demonstrate the technological and scientific feasibility of fusion energy for commercial use.

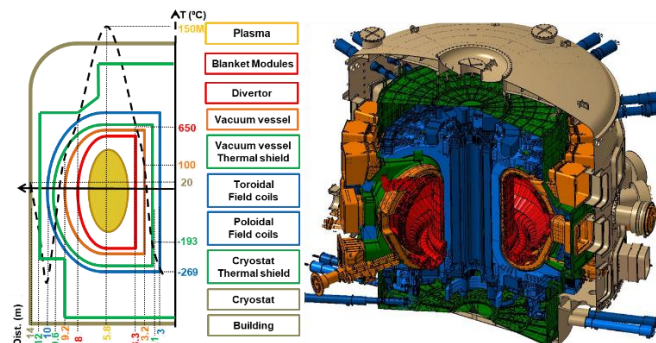


Fig. 1 – ITER tokamak components and associated normal operation temperatures [1].

The ITER Tokamak consists of a superposition of components (Fig. 1), where temperatures range from $150 \times 10^6 \text{K}$ for the plasma core to 4K for the superconductive components at a distance of less than 5m from the core. Although there is a thermal gradient between components, the thermal loads act mainly on the components closest to the plasma. The nuclear fusion reaction heats the components surrounding the plasma via two phenomena, the surface heat

fluxes and neutron fluxes. In order to maintain them down to an acceptable temperature (in general below thermal creep limit), the components are actively cooled with a pressurized fluid (water in most cases) which is one of the design driving loads for the structural integrity [2]. The specificity of a fusion reactor device is the instability of the magneto-hydrodynamics of the plasma, which results in Laplace forces acting on the surrounding structures. These loads are the most severe and cause significant inertial movements of the Vacuum Vessel.

Based on the tritium inventory, the ITER machine has been classified as a Basic Nuclear Installation by French nuclear regulator (INB n°174), which implies that it will be the first fusion reactor to go through a complete nuclear licencing process.

According to ITER materials and analysis experts, the uniqueness of ITER in terms of fusion device under French nuclear licencing imposes the development of a mechanical behaviour model adapted to the most recent material data to respond to the French regulator (ASN) requirements.

1.1 The ITER first confinement barrier

The Vacuum Vessel (VV) is a torus, with several openings on three levels: 18 upper ports, 17 equatorial ports, and 9 lower ports, allowing access for plasma heating, fuelling, diagnostics, and in-vessel component services, see Fig. 2. This doughnut shape is structurally made up of a double wall structure filled with cooling water, to remove the

heat deposited during plasma operation and to maintain a homogeneous temperature.

A maximal cooling water pressure of 1.1 MPa at normal operation (up to 2.4 MPa during baking) classifies it as Nuclear Pressure Equipment (NPE), which requires a third party organisation, i.e., an agreed notified body (ANB), authorized by the nuclear regulator to assure design, fabrication and conformance testing.

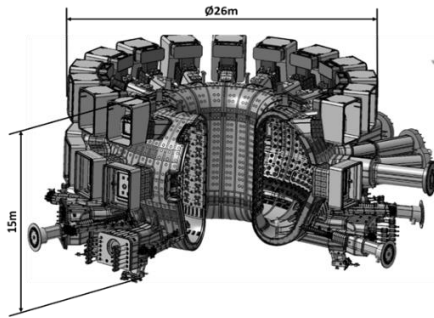


Fig. 2 – ITER Vacuum Vessel.

In addition, the Vacuum Vessel is classified as safety class-1 component according to the ITER classification: this is the primary confinement barrier of the ITER nuclear installation. In order to get licencing of this pressure equipment system by the French regulator (ASN), it has been decided to implement the RCC-MR [3] as the reference design and construction code [4]. This nuclear code provides detailed and basic rules for the design, manufacturing, installation, commissioning and in-service inspection of nuclear plant devices.

The development of the RCC-MR design rules for damage prevention guaranteeing the components' structural integrity, mainly has a dual origin:

- The P-type damage resulting from the application to a structure of a steadily and regularly increasing load or a constant load up to:
 - Ductile damage modes; immediate plastic collapse, immediate plastic instability,
 - Non ductile damage modes; immediate plastic flow localization, immediate local fracture due to ductility exhaustion, fast fracture.
- The S-type damage resulting from repeated applications of load, associated with:
 - Progressive deformations; the permanent overall deformation increases at every loading cycle, inducing additional deformations (i.e., ratcheting) and the structure undergoes gradual changes in its original shape,
 - Fatigue (by progressive cracking); time independent fatigue and time dependent fatigue.

1.2 Ratcheting

As for the finite element analysis, the justification of the structural integrity is made through the elastic route, and when the design criteria cannot be satisfied, several non-linear approaches to the mechanical material behaviour can be considered [5]. The assessment of the cyclic loading conditions cannot be done until the P-type damage criteria are satisfied. In addition to the fatigue damage mode, one of the most difficult design criteria to be satisfied for S-type damage is the ratcheting failure mode.

Two types of ratcheting can be identified: material ratcheting, which is purely related to the material, and structural ratcheting [6].

In tension-compression cyclic loading, many experiments show that metals and alloys undergo variations in their hardening properties during cycles. They may soften or harden depending on the material itself, its temperature, and its initial state. In case of non-symmetric loading with imposed stress, the sample undergoes plastic deformations which can, in the worst case, constantly increase, up to failure mode: this is the material ratcheting, see Fig. 4. Correspondingly, in case of non-symmetric loading with imposed strain condition, the ratcheting is materialised by a relaxation of the mean stress, see Fig. 3 [7].

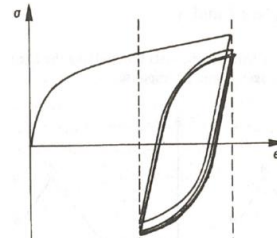


Fig. 3 – Ratcheting: relaxation of the mean stress with imposed strain amplitude [7]

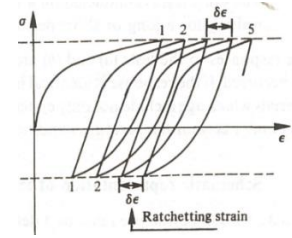


Fig. 4 – Ratcheting: increase in the plastic strain with imposed stress amplitude [7]

Structural ratcheting can occur even without any influence of the material ratcheting. This type of ratcheting is instead governed by the inhomogeneous stress state. This phenomenon can be analysed with simple elastoplastic models [8]. The Bree cylinder is a good representation of a Pressurised Nuclear Equipment (NPE), like the ITER Vacuum Vessel, under operational condition [9]. The Bree cylinder test consists in checking the structural evolution of a tube under constant internal pressure subjected to cyclic thermal loading and is a good representation of structural ratcheting.

The finite element representation of these two cyclic loading phenomena is the core of the work presented in this paper.

2 Mechanical tests on SS316L(N)-IG

Among stainless steel materials, with differences in standards and grades and slight variations in specifications, ITER materials experts have designated a specific ITER material, for which only minor modifications have been made to cope with radiological safety limits and with re-welding requirements [10]. Besides the requirements for good strength, fatigue resistance and adequate ductility to operate under the severe load conditions described in §1, the ITER structural material must also satisfy the requirements for good weldability, resistance to corrosion and vacuum environment compatibility. The main material used in the ITER vacuum vessel, which operates at 100-200°C with expected dose damage below 0.5dpa, is the annealed austenitic stainless steel designated as 316L(N)-IG, as it is readily available and sufficiently strong, see Table 1. The two letters “IG” are for “ITER Grade”.

Table 1 – Main reference properties of SS316L(N)-IG [11]

Temp	Density	Young's Modulus	Poisson's Ratio	Mean Thermal Expansion	Thermal Conductivity	Specific Heat
°C	kg/m ³	GPa		10 ⁻⁶ , 1/K	W/m K	J/kg K
20	7930	200	0.3	15.3	14.28	472
100	7899	193	0.3	15.9	15.48	501
200	7858	185	0.3	16.6	16.98	522

In the literature, plenty of mechanical test results are available for type 316 stainless steel. Nevertheless, to ensure more precise material parameter identification, a mechanical test was performed on a sample machined from a VV base material plate 400x400x40mm.

All tests were performed on a hydraulic traction/compression machine MTS 322 100 kN equipped with an axial MTS extensometer, see Fig. 5.



Fig. 5 –Tensile test machine including extensometer.

2.1 Monotonic tensile test

For the monotonic tensile tests, three specimens were machined in the longitudinal part of the plate and three more in the transversal part. The dimensions are described in Fig. 6.

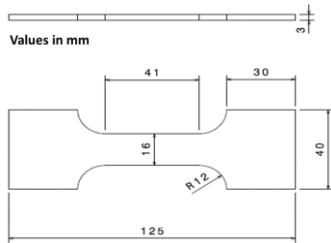


Fig. 6 – Specimen for monotonic tensile test.

The first objective of these tests was to demonstrate that the material is initially isotropic. In addition, some tests were performed to check any evolution of the Young’s modulus after different unloading and reloading phases. No relevant discrepancies were found in the results, see Fig. 7.

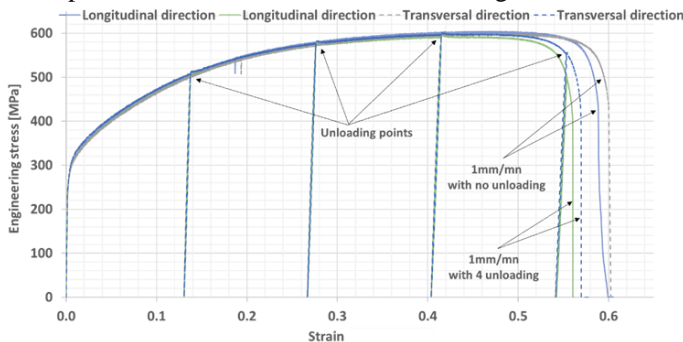


Fig. 7 – Comparison between tensile tests with unloading (#4) and reloading (#4) in transverse and longitudinal direction.

Finally, the viscosity of the material was identified via tests performed at different velocities. It can be observed that at low velocity (1 mm/mn), the ultimate strength was 30% higher in comparison with other tests performed, see Fig. 8.

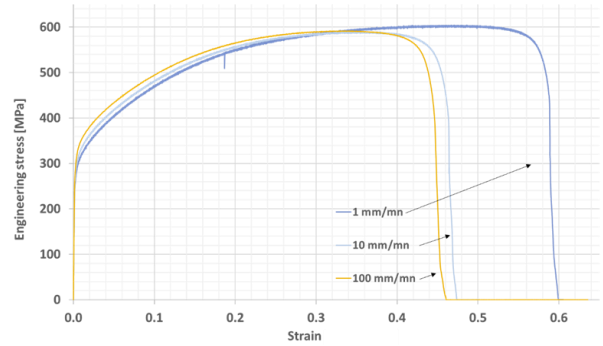


Fig. 8 – Comparison between monotonic tensile tests at different velocities.

2.2 Cyclic tensile/compression test

Since the monotonic tensile tests demonstrated that the material is isotropic, ten additional axisymmetric specimens adapted for cyclic loading were prepared. The dimensions are described in Fig. 9.

The mechanical test campaign performed aimed at highlighting the response of the material to oligocyclic loading. In order to facilitate understanding and interpretation of the results obtained, only two of them are presented in this paper.

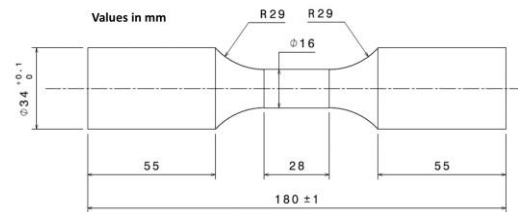


Fig. 9 – Specimen for cyclic test.

From the tensile/compression test, two type of results can be reported, the engineering stress-strain curve, based on the initial cross-section, and the true stress-strain curve, based on the measured cross-section. For our experiments, the extensometer was adapted for measuring the evolution of the test sample diameter, as shown in Fig. 10.

This configuration makes it possible to measure the true stress during imposed force test and to pilot the test in imposed stress. The imposed stress test aims at representing ratcheting, as it is described in section 1.2.

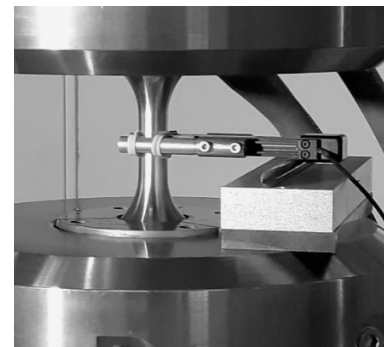


Fig. 10 – Extensometer configuration for cyclic test.

This paper presents two cyclic tension/compression tests, the first of which was made in imposed force, and the second in imposed stress.

In both Fig. 11 and Fig. 13, the orange curve illustrates the engineering stress-strain, and the blue curve the true stress-strain. It is important to note that the initial 10 cycles, which looks like an accommodation phenomenon, is due to the machine initial sequence which gradually reaches the nominal, see point A in Fig. 11 and Fig. 13.

Fig. 11 present the results of a test realised with cyclic force load considering $F_{max}=100kN$ and $F_{min}=-40kN$. The force was imposed following the sinusoidal evolution described in eq.(1), where the mean force $F_{moy}= 30kN$, the force range $\Delta F=140kN$ and the frequency $f=0.3s^{-1}$.

$$F(t) = F_{moy} + \frac{\Delta F}{2} \sin (2 \pi f t) \quad (1)$$

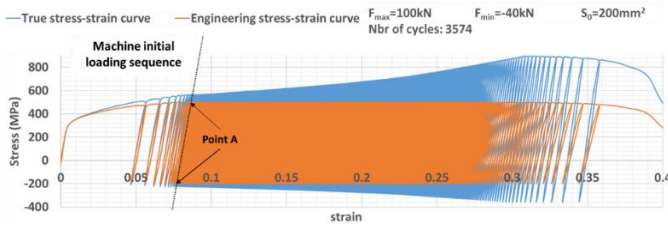


Fig. 11 – Results of cyclic test with imposed force loading

By definition, shakedown appears when the strain evolution between two cycles is equal or close to zero. However, the results show that the strain increases continuously after each cycles. That is why, to dissociate shakedown and ratcheting, we proposed to plot the strain evolution along the cumulative cycles, as it is shown in Fig. 12.

The dashed black line represents the strain evolution with an affine function, for which the slope coefficient provides information on the ratcheting rate. Indeed, when the slope is close to infinite, plastic shakedown occurs, otherwise, ratcheting occurs, see Fig. 12.

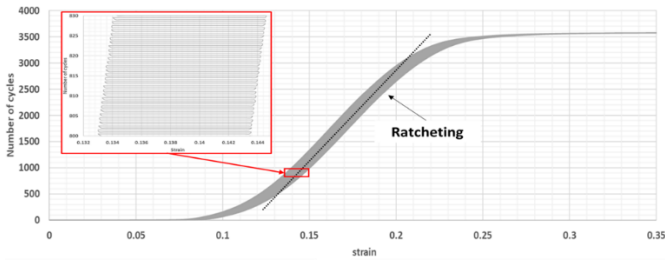


Fig. 12 – Cumulative number of cycles for imposed force loading

Fig. 13 presents the results of a test realised with cyclic stress load considering $\sigma_{max}=780MPa$ and $\sigma_{min}=-300MPa$. The stress was imposed following the same sinusoidal evolution described in eq.(2), where the mean stress $\sigma_{moy}= 240MPa$, the stress range $\Delta\sigma=1080MPa$ and the frequency $f=0.3s^{-1}$.

$$\sigma(t) = \sigma_{moy} + \frac{\Delta\sigma}{2} \sin (2 \pi f t) \quad (2)$$

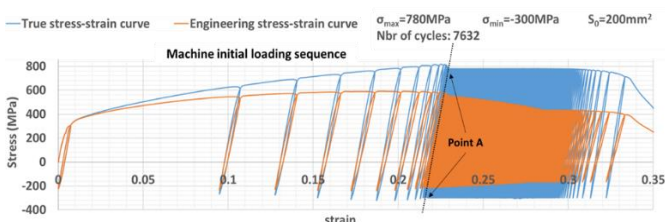


Fig. 13 – Results of cyclic test with imposed stress loading

Obviously, a similar material behaviour than the one for the imposed force test on cyclinder-02 can be observed. This time, however, we have plotted in Fig. 14 the ratcheting strain ($\delta\epsilon$), which is defined in Fig. 4, along the strain from the point A to the end of the test. It shows an exponential evolution that increases rapidly during the last 10 cycles.

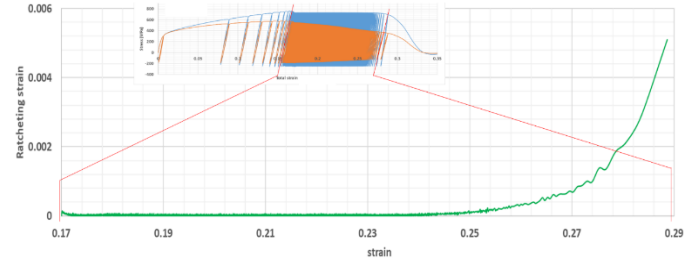


Fig. 14 – Ratcheting strain along the strain for imposed stress loading

The macroscopic views of the cyclic test sample presented in Fig. 15 show a ductile fracture on the periphery and a brittle fracture in the centre, occurring after 3574 cycles in cyclic force loading and after 7632 cycles in cyclic stress loading.

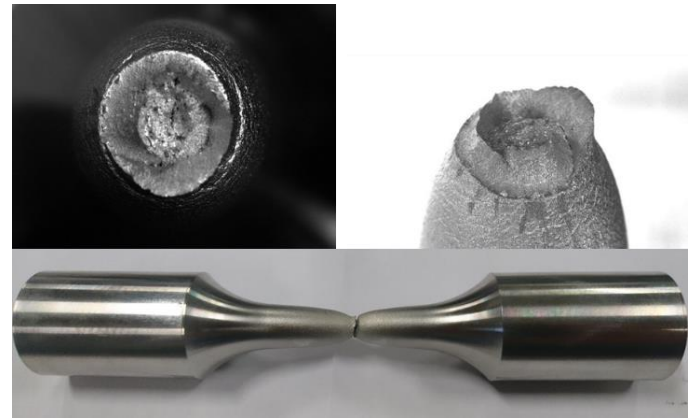


Fig. 15 – Macroscopic view of the specimen after rupture

At this step, the challenge is to represent the observed test material behaviour through a phenomenological approach.

3 Development of a non-linear thermo-mechanical behaviour model

In the general case, the model development is based on the superposition of several hardening functions in order to represent the complex phenomena that can be observed in the different (thermo)mechanical tests [7].

For the sake of being as close as possible to the real material behaviour, and with the objective of defining a reasonable number of state variables, it is mandatory to identify the environment in which the model would be used. In the present case, the proposed model would have to represent the following hardening behaviours:

- Bauschinger effect,
- cyclic softening and hardening,
- shakedown (elastic and/or plastic),
- ratcheting,
- damage, i.e., formation and growth of microcavities (micropores).

Although the strain levels recorded during the experimental tests exceed 50%, the tensor of the infinitesimal strain will be retained as the basic kinematic variable in the model. By following the nuclear design rules, it is excluded that the VV structural material can undergo large deformations, which are nevertheless not required for plastic shakedown and ratcheting to occur. The stress and strain fields in the VV under normal operation conditions will be heterogeneous, and this heterogeneity may be sufficient to trigger these phenomena, even though the deformations remain, globally and locally, well below 50%.

3.1 State variables & state potential

The two basic state variables that should necessarily be considered when dealing with thermomechanical problems are the absolute temperature $T \in \mathbb{R}^+$ (in K) and, in the cases where the deformations of the material remain “small”, the infinitesimal strain tensor $\boldsymbol{\varepsilon} \in \mathbb{R}^3 \times \mathbb{R}^3$ (unitless). However, as soon as the behaviour of the material is no longer thermo-elastic, other state variables, usually called “internal” (state) variables, [12], must be added to T and $\boldsymbol{\varepsilon}$, to take into account different irreversible mechanisms, such as permanent strain, hardening and damage. In the present study, these additional variables are:

- $\boldsymbol{\varepsilon}^p \in \mathbb{R}^3 \times \mathbb{R}^3$: plastic strain tensor (unitless),
- $\mathbf{X}_i \in \mathbb{R}^3 \times \mathbb{R}^3$: i^{th} kinematic hardening tensor (unitless),
- $p \in \mathbb{R}^+$: isotropic hardening variable (unitless),
- $d \in [0,1]$: damage variable (unitless).

We also assume that the plastic flow is incompressible, therefore $\text{Tr}(\boldsymbol{\varepsilon}^p)=0$ and $\text{Tr}(\mathbf{X}_i)=0$.

The Helmholtz free energy density Ψ (in J/kg) is taken as thermodynamic potential, corresponding to a function of all state variables. We assume the following expression for the development of the constitutive model:

$$\begin{aligned} \Psi(T, \boldsymbol{\varepsilon}, \boldsymbol{\varepsilon}^p, \mathbf{X}_i, p, d) = & \\ & + \frac{1}{2\rho_0} \lambda (\text{Tr}(\boldsymbol{\varepsilon} - \boldsymbol{\varepsilon}^p))^2 + \mu (\boldsymbol{\varepsilon} - \boldsymbol{\varepsilon}^p) : (\boldsymbol{\varepsilon} - \boldsymbol{\varepsilon}^p) \\ & - \frac{1}{\rho_0} (3\lambda + 2\mu) \gamma \text{Tr}(\boldsymbol{\varepsilon} - \boldsymbol{\varepsilon}^p) (T - T_0) \\ & - \frac{C_\varepsilon (T - T_0)^2}{2T_0} \\ & + \frac{1}{\rho_0} k (1 - d) \left(p + \frac{1}{m} e^{-mp} \right) \\ & + \frac{1}{2\rho_0} \sum_{i=1}^{N_{kh}} M_i \mathbf{X}_i : \mathbf{X}_i \end{aligned} \quad (3)$$

where ρ_0 (in kg.m^{-3}) is the initial density, T_0 is the initial temperature and $\text{Tr}(\cdot)$ is the trace operator. λ , μ , γ , C_ε , M_i , k and m are material parameters (temperature dependent), which should be identified from experimental results, such as monotonic and cyclic tension-compression test results.

The first part of the free energy represents the mechanical part of the linear elastic deformation which is dependent on the material parameters λ (in Pa) and μ (in Pa), first and second Lamé coefficients.

$$\rho_0 \bar{\Psi}_{\boldsymbol{\varepsilon}^e}^1(\boldsymbol{\varepsilon}, \boldsymbol{\varepsilon}^p) = \frac{\lambda}{2} (\text{Tr}(\boldsymbol{\varepsilon} - \boldsymbol{\varepsilon}^p))^2 + \mu \text{Tr}((\boldsymbol{\varepsilon} - \boldsymbol{\varepsilon}^p) : (\boldsymbol{\varepsilon} - \boldsymbol{\varepsilon}^p)) \quad (4)$$

Obviously, plastic strain $\boldsymbol{\varepsilon}^p$, elastic strain $\boldsymbol{\varepsilon}^e \in \mathbb{R}^3 \times \mathbb{R}^3$ (unitless) and total strain $\boldsymbol{\varepsilon}$ can be linked via the following equation:

$$\boldsymbol{\varepsilon} = \boldsymbol{\varepsilon}^e + \boldsymbol{\varepsilon}^p \Leftrightarrow \boldsymbol{\varepsilon}^e = \boldsymbol{\varepsilon} - \boldsymbol{\varepsilon}^p \quad (5)$$

The second part of the free energy represents the thermoelastic part where γ (in K^{-1}) is the thermal expansion parameter:

$$\rho_0 \bar{\Psi}_{\boldsymbol{\varepsilon}^e}^2(\boldsymbol{\varepsilon}, \boldsymbol{\varepsilon}^p, T) = -(3\lambda + 2\mu) \gamma \text{Tr}(\boldsymbol{\varepsilon} - \boldsymbol{\varepsilon}^p) (T - T_0) \quad (6)$$

The purely thermal effects are obviously taken into account in the model, via the third part of the free energy, including the heat capacity C_ε (in J/kg.K):

$$\bar{\Psi}_T(T) = -\frac{C_\varepsilon (T - T_0)^2}{2T_0} \quad (7)$$

This form makes it possible to obtain a linear temperature dependency of the heat capacity, as observed experimentally [11].

The kinematic hardening represents the non-homogeneous plastic deformation linked to the characteristic coefficient of the material M_i (in Pa). The kinematic hardening is commonly represented by summing several variables \mathbf{X}_i (where $N_{kh}=2$ or 3 in most cases) aiming at smoothing the plastic behaviour in order to obtain a better agreement with experiments. The superposition of kinematic variables is made by summing the different terms as follows, to represent the kinematic hardening part of the free energy [13]:

$$\rho_0 \bar{\Psi}_X(\mathbf{X}_i) = \frac{1}{2} \sum_{i=1}^{N_{kh}} M_i \mathbf{X}_i : \mathbf{X}_i \quad (8)$$

It has been observed from the cyclic tension-compression tests that the material exhibits a hardening behaviour with a logarithmic trend. We propose a non-linear expression of the isotropic hardening (e.g. [13]), where m (unitless) and k (in Pa) are two characteristic coefficients of the material. For an undamaged material, the expression of the free energy representing the isotropic hardening can be defined as:

$$\rho_0 \bar{\Psi}_p(p) = k \left(p + \frac{1}{m} e^{-mp} \right) \quad (9)$$

The modelling of ductile fracture in the framework of continuum damage mechanics is resulting from the competition between hardening and damage. The damage variable is based on the concept that ductile fracture results from the formation, growth and coalescence of cavities, see Fig. 16 [14]. Despite the complexity of this damage mechanism, the chosen hypothesis assumes only one single type of cavity with isotropic evolution.

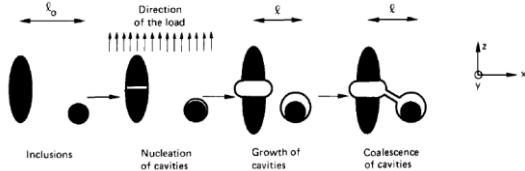


Fig. 16 – Modelling of ductile fracture [5].

On the assumption that this phenomenon is isotropic, the surface density of these microcracks and microcavities can be represented by a scalar variable d , where $d=0$ in the undamaged state and $d=1$ when the exhaustion of ductility is reached [14]. Fig. 17 illustrates an example of the damage variable evolution [15].

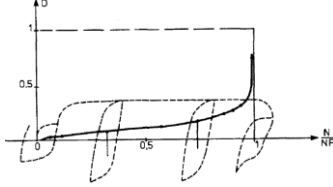


Fig. 17 –Example of the damage evolution during a low cycle creep fatigue test [15]

For a damaged material, a competition is assumed to exist between plasticity (trend to positive hardening) and damage (trend to negative hardening). Consequently, eq.(9) is modified in the following way:

$$\rho_0 \bar{\Psi}_p(p, d) = (1 - d)k \left(p + \frac{1}{m} e^{-mp} \right) \quad (10)$$

It is important to note that all material parameters can be temperature dependent. Nevertheless, to simplify the following equations in this paper, this dependence will be neglected on the hypothesis that the temperature range studied has no significant effect (<5%).

In addition, the identification of the parameters, including the temperature dependence, requires a large and complex set of test campaign results, which are not part of this paper.

3.2 Expression of intrinsic dissipation

The first law of the thermodynamics first postulates that an internal energy can be defined for all thermodynamics systems and, secondly, that the variation of this internal energy is ever equal to that of energy supplied to the system as heat (thermal part) and work (mechanical part). In continuum thermodynamics, it reads:

$$\rho_0 T \dot{s} + \text{div}(\mathbf{q}) - r^v = \boldsymbol{\sigma} : \dot{\boldsymbol{\varepsilon}} - \rho_0 \dot{\Psi} - \rho_0 s \dot{T} \quad (11)$$

where s is the entropy density (J/kg.K), \mathbf{q} is the the surface heat fluxes (W/m²), and r^v is the external heat source (W/m³).

The second law of thermodynamics first state that an entropy can be defined for all thermodynamic systems and, secondly, that he variation of the entropy is ever greater or equal to that of the surroundings of the system. In continuum thermodynamics, it reads:

$$\rho \dot{s} + \text{div} \left(\frac{\mathbf{q}}{T} \right) - \frac{r^v}{T} \geq 0 \quad (12)$$

This evolution is the sum of the thermal dissipation (heat conduction) and the intrinsic dissipation, which are both assumed positive or null. The expression of intrinsic dissipation Φ_{int} (W/m³) is function of the expression of the free energy derivative, expressed as (see [12]):

$$\begin{aligned} \Phi_{int} = & \left(\boldsymbol{\sigma} - \rho_0 \frac{\partial \Psi}{\partial \boldsymbol{\varepsilon}} \right) : \dot{\boldsymbol{\varepsilon}} - \rho_0 \left(s + \frac{\partial \Psi}{\partial T} \right) \dot{T} \\ & - \rho_0 \frac{\partial \Psi}{\partial \boldsymbol{\alpha}} \cdot \dot{\boldsymbol{\alpha}} \geq 0 \end{aligned} \quad (13)$$

where $\boldsymbol{\alpha}$ is a synthetic representation of the set of the internal variables (p , d , $\boldsymbol{\varepsilon}^p$ and \mathbf{X}_i , in the present study).

Due to the fact that the entropy density is a state function, a first condition for the non negativity of the intrinsic dissipation, see eq.(13) is

$$s = - \frac{\partial \Psi}{\partial T} \quad (14)$$

Furthermore, and in agreement with all experimental testing made on the VV structural material (see §2), the viscoelastic phenomena will not be taken into account in the present study. The stress tensor $\boldsymbol{\sigma}$ can then be considered as a state function, which can be written as follows:

$$\boldsymbol{\sigma} = \rho_0 \frac{\partial \Psi}{\partial \boldsymbol{\varepsilon}} \quad (15)$$

As it is stated at the end of §3.1, to simplify the following equations, the dependence of the material parameters on temperature is omitted.

Using eq. (3), we can explicitly express the stress and the entropy density for our model:

$$\begin{aligned} \boldsymbol{\sigma} = & \rho_0 \frac{\partial \Psi}{\partial \boldsymbol{\varepsilon}} = \\ & \lambda \text{Tr}(\boldsymbol{\varepsilon} - \boldsymbol{\varepsilon}^p) \mathbf{G} + 2\mu(\boldsymbol{\varepsilon} - \boldsymbol{\varepsilon}^p) \\ & - (3\lambda + 2\mu)\gamma(T - T_0) \mathbf{G} \end{aligned} \quad (16)$$

where \mathbf{G} is the metric tensor (in any orthonormal basis, $G_{ij} = \delta_{ij}$ where δ_{ij} represents the Kronecker delta).

$$\begin{aligned} s = & - \frac{\partial \Psi}{\partial T} = \\ & \frac{C_\varepsilon(T - T_0)}{T_0} + \frac{(3\lambda + 2\mu)\gamma \text{Tr}(\boldsymbol{\varepsilon} - \boldsymbol{\varepsilon}^p)}{\rho_0} \end{aligned} \quad (17)$$

The partial derivative of Ψ with respect to the internal variables can be developed as:

$$\begin{aligned} \rho_0 \frac{\partial \Psi}{\partial \boldsymbol{\alpha}} \cdot \dot{\boldsymbol{\alpha}} = & \rho_0 \frac{\partial \Psi}{\partial p} \dot{p} + \rho_0 \frac{\partial \Psi}{\partial d} \dot{d} + \\ & \rho_0 \frac{\partial \Psi}{\partial \boldsymbol{\varepsilon}^p} : \dot{\boldsymbol{\varepsilon}}^p + \rho_0 \sum_{i=1}^{N_{kh}} \frac{\partial \Psi}{\partial \mathbf{X}_i} : \dot{\mathbf{X}}_i \end{aligned} \quad (18)$$

Consequently, the expression of the intrinsic dissipation is:

$$\begin{aligned} \Phi_{int} = & \rho_0 \frac{\partial \Psi}{\partial p} \dot{p} + \rho_0 \frac{\partial \Psi}{\partial d} \dot{d} + \rho_0 \frac{\partial \Psi}{\partial \boldsymbol{\varepsilon}^p} : \dot{\boldsymbol{\varepsilon}}^p \\ & + \rho_0 \sum_{i=1}^{N_{kh}} \frac{\partial \Psi}{\partial \mathbf{X}_i} : \dot{\mathbf{X}}_i \geq 0 \end{aligned} \quad (19)$$

The expression of the partial derivative of Ψ with respect to the plastic strain ($\boldsymbol{\varepsilon}^p$) gives us the thermodynamical

force $\mathbf{A}^{\varepsilon^p}$ associated with the plastic strain (the minus sign is conventional):

$$\mathbf{A}^{\varepsilon^p} = -\rho_0 \frac{\partial \Psi}{\partial \boldsymbol{\varepsilon}^p} = \rho_0 \frac{\partial \Psi}{\partial \boldsymbol{\varepsilon}} = \boldsymbol{\sigma} \quad (20)$$

The expression of the partial derivative of Ψ with respect to the i^{th} tensor variable of kinematic hardening (\mathbf{X}_i), gives us the i^{th} thermodynamical force $\mathbf{A}^{\mathbf{X}_i}$ associated with the kinematic hardening:

$$\mathbf{A}^{\mathbf{X}_i} = -\rho_0 \frac{\partial \Psi}{\partial \mathbf{X}_i} = -M_i \mathbf{X}_i \quad (21)$$

The isotropic function R including the damage variable is defined by the partial derivative of Ψ with respect to the isotropic variable (p):

$$A^p = -\rho_0 \frac{\partial \Psi}{\partial p} = -k(1-d)(1-e^{-mp}) \quad (22)$$

The partial derivative of Ψ with respect to the damage variable (d) is:

$$A^d = -\rho_0 \frac{\partial \Psi}{\partial d} = k \left(p + \frac{1}{m} e^{-mp} \right) \quad (23)$$

With all these expressions, we should formulate evolution equations that will ensure the positivity of the intrinsic dissipation whatever the state ($T, \boldsymbol{\varepsilon}, \boldsymbol{\varepsilon}^p, \mathbf{X}_i, p, d$) and whatever \dot{T} and $\dot{\boldsymbol{\varepsilon}}$.

3.3 Evolution equations of internal variables

The internal variables start to evolve when the irreversible deformations occurs. The Von Mises criterion was selected to express the elastic threshold as it is described in [7], at the difference that this criterion would be dependent on the damage variable d .

Taking into account the expression of the isotropic hardening function R eq. (22), the expression of the elastic threshold function appears as:

$$f(\boldsymbol{\sigma}, \mathbf{A}^{\mathbf{X}_i}, A^p, A^d) = J \left(\boldsymbol{\sigma} + \sum_{i=1}^{N_{kh}} \mathbf{A}^{\mathbf{X}_i} \right) - A^p - \sigma_0 \quad (24)$$

where σ_0 (in MPa) is the initial yield limit, and the equivalent stress tensor in the sense of Von Mises is expressed as:

$$J(\boldsymbol{\sigma}) = \sqrt{\frac{3}{2} \mathbf{Dev}(\boldsymbol{\sigma}) : \mathbf{Dev}(\boldsymbol{\sigma})} \quad (25)$$

where $\mathbf{Dev}(\cdot)$ is the deviatoric operator described as:

$$\mathbf{Dev}(\boldsymbol{\sigma}) = \boldsymbol{\sigma} - \frac{1}{3} \text{Tr}(\boldsymbol{\sigma}) \mathbf{G} \quad (26)$$

The evolution equations of the internal variables must be such that the inequality concerning the intrinsic dissipation, see eq.(19), is ever satisfied. The framework of the so called generalised standard materials, e.g. [16], allows

the systematic verification of this constraint. It is based on two assumption, namely:

- i) a plastic multiplier Λ can be defined, which cannot be negative,
- ii) at least one plastic flow potential can be defined, whose partial derivative fix the direction for the evolution of the internal variables.

As a consequence of i) and ii), the evolution equations for the set of internal variables $\boldsymbol{\alpha}$, see eq.(13), read:

$$\dot{\boldsymbol{\alpha}} = \Lambda \frac{\partial g}{\partial \mathbf{A}^\alpha} \quad (27)$$

In the present paper, due to the fact that plasticity and damage are irreversible phenomena that can evolve in very different ways, two flow potentials are clearly distinguished, one for the plasticity, g , and one for the damage, g^d . The intrinsic dissipation then reads:

$$\begin{aligned} \vartheta_{int} = -\rho_0 \left(\frac{\partial \Psi}{\partial \boldsymbol{\varepsilon}^p} : \Lambda \frac{\partial g}{\partial \boldsymbol{\sigma}} + \frac{\partial \Psi}{\partial p} \Lambda \frac{\partial g}{\partial A^p} + \sum_{i=1}^{N_{kh}} \left(\frac{\partial \Psi}{\partial \mathbf{X}_i} : \dot{\mathbf{X}}_i \right) : \Lambda \frac{\partial g}{\partial \mathbf{A}^{\mathbf{X}_i}} \right. \\ \left. + \frac{\partial \Psi}{\partial d} \Lambda \frac{\partial g^d}{\partial A^d} \right) \end{aligned} \quad (28)$$

For representing the ratcheting response, the equation setting requires the use of a non-associative model where the plastic flow potential g is not only defined by the expression of the elastic threshold function eq.(24), but also with an additional term initially described by Armstrong and Frederick as follow [17]:

$$\begin{aligned} g(\boldsymbol{\sigma}, \mathbf{A}^{\mathbf{X}_i}, A^p, A^d) = \\ f(\boldsymbol{\sigma}, \mathbf{A}^{\mathbf{X}_i}, A^p, A^d) \\ + \sum_{i=1}^{N_{kh}} \left(\frac{\Gamma_i}{2M_i} (\mathbf{Dev}(\mathbf{X}_i) : \mathbf{Dev}(\mathbf{X}_i)) \right) \end{aligned} \quad (29)$$

where Γ_i are unitless material parameters.

This additional term, which is linked to the ratcheting strains, see Fig. 4, is too pronounced, and most of the past studies performed in the objective of minimising this material response have conducted to the introduction of additional parameters inducing a more complex elaboration of the material behaviour law see [18], [19], [20], [21], [22], [23] and [24].

We have observed during the mechanical test campaign that after each cycle, the specimen is evolving, and the only difference between the stabilised response and the ratcheting is the ratcheting strain value ($\delta \boldsymbol{\varepsilon}$) between each cycle. Moreover, for tension-compression tests conducted in imposed stress, we have observed that the ratcheting strain have an exponential evolution that increases rapidly during the last 10 cycles, as it is described in Fig. 14.

As the ratcheting failure mode is induced by a ductile fracture, and as the damage variable evolution proposed by Lemaitre [15] and Rousselier [14] in continuum damage mechanics adopts an exponential behaviour similar to the one experimentally observed in Fig. 17. We propose a coupling between the damage variable and the plastic flow potential as follow:

$$\begin{aligned} g(\boldsymbol{\sigma}, \mathbf{A}^{\mathbf{X}_i}, A^p, A^d) = \\ f(\boldsymbol{\sigma}, \mathbf{A}^{\mathbf{X}_i}, A^p, A^d) \\ + d \sum_{i=1}^{N_{kh}} \left(\frac{\Gamma_i}{2M_i} (\mathbf{Dev}(\mathbf{X}_i) : \mathbf{Dev}(\mathbf{X}_i)) \right) \end{aligned} \quad (30)$$

This additional coupling with the damage variable ensures that ratcheting strain evolution is minimised at low damage mode, i.e. when d is close to 0, whereas when d is close to 1, $\delta\epsilon$ is high enough to generate ratcheting response.

The second flow potential g^d is dedicated to the damage variable evolution and decoupled from main plastic flow potential g . On the assumption that the microcrack propagation is isotropic and the growth of cavities depends on the tensile loading only, this plastic flow is function of the positive part of the stress tensor and the damage variable. This flow potential is adjusted by a characteristic coefficient of the material, n (in Pa). Finally, to ensure that the variable d will not exceed 1, we have introduced the term $(1-d)$ that sets the variable evolution to zero as soon as $d=1$. The flow potential g^d can be expressed as follows:

$$g^d = \frac{d}{n} (1-d) \langle Tr(\sigma) \rangle A^p \quad (31)$$

Let us express the evolution of all variables based on the partial derivatives of the plastic flow potential g , starting with the derivative with respect to the plastic strain (ϵ^p):

$$\dot{\epsilon}^p = \Lambda \frac{\partial g}{\partial \sigma} = \Lambda \left(\frac{3}{2J(\sigma - \sum_{i=1}^{N_{kh}} M_i X_i)} \right) \cdot Dev \left(\sigma - \sum_{i=1}^{N_{kh}} M_i X_i \right) \quad (32)$$

The evolution of the tensor variable of kinematic hardening (X_i) can be expressed as:

$$\dot{X}_i = \Lambda \frac{\partial g}{\partial A^i} = \dot{\epsilon}^p - d \Lambda \Gamma_i Dev(X_i) \quad (33)$$

The evolution of the isotropic variable (p) can be expressed as:

$$\dot{p} = \Lambda \frac{\partial g}{\partial A^p} = \Lambda \quad (34)$$

The evolution of the damage variable is defined by the following equation:

$$\dot{d} = \Lambda \frac{\partial g^d}{\partial A^d} = \Lambda \frac{d(1-d)}{n} \langle Tr(\sigma) \rangle \quad (35)$$

On the assumption that the microcrack propagation is isotropic and the growth of cavities depends on the tensile loading only, [14], eq.(35) involves Mc Cauley brackets defined as:

$$\langle Tr(\sigma) \rangle = \begin{cases} 0 & \text{if } Tr(\sigma) < 0 \\ Tr(\sigma) & \text{if } Tr(\sigma) \geq 0 \end{cases} \quad (36)$$

A strictly positive value is required for the internal damage variable to initiate damage evolution (from eq.(35)) we see that $\dot{d} = 0$ if $d(=0)=d_0(=0)$. It is proposed to set the parameter d_0 at a value between 10^{-4} and 10^{-5} , which corresponds to the initial fraction of cavities. The evolution of the cavities will mainly be driven by the plastic flow multiplier Λ and it will be adjusted by a characteristic coefficient of the material, n (in Pa).

With the assumption proposed here, only the viscoplastic behaviour, which is by definition function of

time, will be studied. These kinds of models can represent creep and relaxation, which is why the model proposed by Perzyna (see [25]) to represent the viscoplasticity behaviour was selected.

It is necessary to propose an expression for $\Lambda \geq 0$ where η (in s) is characteristic coefficient of the material:

$$\Lambda = \frac{1}{\eta} \left(\frac{J(\sigma - \sum_{i=1}^{N_{kh}} M_i X_i) - A^p - \sigma_0}{\sigma_0} \right) \quad (37)$$

All the terms in the expression of the intrinsic dissipation eq.(28) have now been developed, and the new expression appears as:

$$\Lambda \left(\begin{array}{l} \varnothing_{int} = \\ J \left(\sigma - \sum_{i=1}^{N_{kh}} M_i X_i \right) + d \sum_{i=1}^{N_{kh}} M_i \Gamma_i Dev(X_i) : Dev(X_i) \\ - k(1-d)(1-e^{-mp}) \\ + \frac{d(1-d)}{n} \langle Tr(\sigma) \rangle k \left(p + \frac{1}{m} e^{-mp} \right) \end{array} \right) \quad (38)$$

It can be shown that eq.(38) is always positive or null whatever is the thermodynamical state.

3.4 Expression of the heat equation (first thermodynamic principle for this model)

The evolution of the entropy density \dot{s} can be deduced by derivating the expression of eq. (17):

$$\dot{s} = C_\epsilon \frac{\dot{T}}{T_0} + \frac{(3\lambda + 2\mu)\gamma Tr(\dot{\epsilon})}{\rho_0} \quad (39)$$

The thermal conduction in a homogeneous volume can be expressed with the Fourier's law, which states that the internal heat generation flux is proportional to the temperature gradient. According to the isotropic Fourier's law, this flux distribution is expressed as follow:

$$div(\mathbf{q}) = -k \cdot div(grad(T)) = -k_T \Delta T \quad (40)$$

where k_T is the heat conductivity coefficient.

Starting from the first law, eq.(11), and the second law, eq.(13), of thermodynamics, and taking into account the expression of the intrinsic dissipation, eq.(38), the entropy density evolution, eq.(41), and the flux distribution, eq.(40), the heat equation for this model can be written as follows:

$$\begin{aligned} & \frac{\rho_0 C_\epsilon}{T_0} T \dot{T} - k_T \Delta T - r^v \\ & = \\ & -(3\lambda + 2\mu)\gamma Tr(\dot{\epsilon}) T \\ & + \Lambda J \left(\sigma - \sum_{i=1}^{N_{kh}} M_i X_i \right) \\ & + d \sum_{i=1}^{N_{kh}} M_i \Gamma_i Dev(X_i) : Dev(X_i) \\ & + k \Lambda (1-d)(1-e^{-mp}) \\ & + \left(k \left(p + \frac{1}{m} e^{-mp} \right) \right) \Lambda \frac{d(1-d)}{n} \langle Tr(\sigma) \rangle \end{aligned} \quad (41)$$

The strong thermo-mechanical coupling requires the heat equation described in eq.(41) be solved together with the balance of linear momentum (Cauchy's first law of motion or motion equations) described as:

$$\mathbf{Div}(\boldsymbol{\sigma}) + \mathbf{f}^p = \mathbf{0} \quad (42)$$

where \mathbf{f}^p are the body forces. These equilibrium equations must be completed with appropriate initial and boundary conditions. An application of this strong thermo-mechanical coupling is presented in section 6.

4 Model predictions in some simple loading case ("0D" simulations)

In order to illustrate the ability of the proposed model to represent the specific characteristic for which it was developed, it was tested on homogeneous problems. We considered the case of a cyclic homogeneous uniaxial tensile test with a strong thermo-mechanical coupling. For this, all variables that are involved in non-linear ordinary differential equation (ODE)s were solved using MATLAB[®] software.

4.1 Hypothesis for cyclic uniaxial tensile test

In order to simplify the resolution of the heat and mechanical equations, the following hypotheses were made:

- no body forces: $\mathbf{f}^v=0$,
- the stress distribution is uniform: $\mathbf{div}(\boldsymbol{\sigma})=0$,
- the temperature distribution is uniform: $\text{grad}(T)=0$ and $k\Delta T=0$,
- no volumic heat generation applied: $r^v=0$,
- uniaxial loading: $\sigma_{22}=\sigma_{33}=0$ and $\varepsilon_{22}=\varepsilon_{33}$,

The input signal is an imposed stress along the direction \mathbf{e}_1 where the stress tensor is defined in a given orthonormal basis ($\mathbf{e}_1, \mathbf{e}_2, \mathbf{e}_3$) as:

$$[\boldsymbol{\sigma}(t)] = \begin{bmatrix} \sigma_{11}(t) & 0 & 0 \\ 0 & 0 & 0 \\ 0 & 0 & 0 \end{bmatrix} \quad (43)$$

The deviatoric part of $\boldsymbol{\sigma}$ is thus given by:

$$[\text{Dev}\boldsymbol{\sigma}(t)] = \begin{bmatrix} \frac{2}{3}\sigma_{11}(t) & 0 & 0 \\ 0 & -\frac{1}{3}\sigma_{11}(t) & 0 \\ 0 & 0 & -\frac{1}{3}\sigma_{11}(t) \end{bmatrix} \quad (44)$$

In the same orthonormal basis ($\mathbf{e}_1, \mathbf{e}_2, \mathbf{e}_3$), the total strain tensor, the plastic strain tensor and the kinematic hardening tensors are defined as:

$$[\boldsymbol{\varepsilon}(t)] = \begin{bmatrix} \varepsilon_{11}(t) & 0 & 0 \\ 0 & \varepsilon_{22}(t) & 0 \\ 0 & 0 & \varepsilon_{22}(t) \end{bmatrix} \quad (45)$$

$$[\boldsymbol{\varepsilon}^p(t)] = \begin{bmatrix} \varepsilon_{11}^p(t) & 0 & 0 \\ 0 & \varepsilon_{22}^p(t) & 0 \\ 0 & 0 & \varepsilon_{22}^p(t) \end{bmatrix} \quad (46)$$

$$[X_{(i)}(t)] = \begin{bmatrix} X_{(i)11}(t) & 0 & 0 \\ 0 & X_{(i)22}(t) & 0 \\ 0 & 0 & X_{(i)22}(t) \end{bmatrix} \quad (47)$$

4.2 First order differential equations

The objective is to express the evolution of the strain tensor relative to the stress tensor according to the evolution of the other variables. From eq.(16), the stress tensor components can be expressed as:

$$\begin{cases} \sigma_{11} = \lambda \text{Tr}(\boldsymbol{\varepsilon}) + 2\mu(\varepsilon_{11}) - 2\mu(\varepsilon_{11}^p) - Th_{11} \\ 0 = \lambda \text{Tr}(\boldsymbol{\varepsilon}) + 2\mu(\varepsilon_{22}) - 2\mu(\varepsilon_{22}^p) - Th_{22} \\ 0 = \lambda \text{Tr}(\boldsymbol{\varepsilon}) + 2\mu(\varepsilon_{22}) - 2\mu(\varepsilon_{22}^p) - Th_{33} \end{cases} \quad (48)$$

where the thermal part of the stress tensor is defined as:

$$Th_{11} = Th_{22} = Th_{33} = (3\lambda + 2\mu)\gamma(T - T_0) \quad (49)$$

Starting from eq. (48), the expression of the total strain along the direction \mathbf{e}_1 appear as:

$$\varepsilon_{11} = \frac{1}{2\mu}\sigma_{11} - \frac{1}{2\mu}\text{Tr}(\boldsymbol{\varepsilon}) + \frac{1}{2\mu}Th_{11} + \varepsilon_{11}^p \quad (50)$$

Additionally, the expression of trace of the total strain tensor can be deduced from eq. (48):

$$\text{Tr}(\boldsymbol{\varepsilon}) = \frac{1}{3\lambda + 2\mu}\sigma_{11} + 3\gamma(T - T_0) \quad (51)$$

After some calculations, the expression of the total strain evolution along the \mathbf{e}_1 axis and the trace of the total strain tensor evolution appears as:

$$\text{Tr}(\dot{\boldsymbol{\varepsilon}}) = \frac{1}{3\lambda + 2\mu}\dot{\sigma}_{11} + 3\gamma\dot{T} \quad (52)$$

The differential equations involving the evolution of the plastic strain tensor along the loaded and transversal axis are respectively:

$$\dot{\varepsilon}_{11}^p = \frac{3}{2J(\boldsymbol{\sigma} - \sum_{i=1}^2 M_i X_i)} \cdot \left((\text{Dev}\boldsymbol{\sigma})_{11} - \sum_{i=1}^2 M_i (\text{Dev}X_{(i)})_{11} \right) \dot{p} \quad (53)$$

$$\dot{\varepsilon}_{22}^p = \frac{3}{2J(\boldsymbol{\sigma} - \sum_{i=1}^2 M_i X_i)} \cdot \left((\text{Dev}\boldsymbol{\sigma})_{22} - \sum_{i=1}^2 M_i (\text{Dev}X_{(i)})_{22} \right) \dot{p} \quad (54)$$

The differential equation involving the evolution of the tensorial variable of kinematic hardening along the \mathbf{e}_1 axis and the \mathbf{e}_2 axis are respectively:

$$\dot{X}_{(i)11} = \dot{\varepsilon}_{11}^p - \dot{p}d\Gamma_i(\text{Dev}X_{(i)})_{11} \quad (55)$$

$$\dot{X}_{(i)22} = \dot{\varepsilon}_{22}^p - \dot{p}d\Gamma_i(\text{Dev}X_{(i)})_{22} \quad (56)$$

The differential equation involving the evolution of the isotropic hardening is:

$$\dot{p} = \frac{1}{\eta} \left(\frac{J(\boldsymbol{\sigma} - \sum_{i=1}^2 M_i X_i) - R(p, d) - \sigma_0}{\sigma_0} \right)^\alpha \quad (57)$$

The differential equation involving the evolution of the damage is:

$$\dot{d} = \dot{p} \frac{d}{n} (1-d) \langle \sigma_{11}(t) \rangle \quad (58)$$

The differential equation involving the evolution of temperature is:

$$\begin{aligned} \dot{T} = & \left(\frac{T_0}{\rho_0 T C_\varepsilon} \right) r^v - \frac{(3\lambda + 2\mu) \gamma T r(\dot{\epsilon}) T_0}{\rho C_\varepsilon} \\ & + \left(\frac{T_0}{\rho_0 T C_\varepsilon} \right) \dot{p} \left(J \left(\sigma - \sum_{i=1}^2 M_i X_i \right) - R \right) \\ & + \left(\frac{T_0}{\rho_0 T C_\varepsilon} \right) \dot{p} \left(d \sum_{i=1}^2 \Gamma_i M_i \text{Dev}(X_i) : \text{Dev}(X_i) \right) \\ & + \left(\frac{T_0}{\rho_0 T C_\varepsilon} \right) \dot{p} \left(p + \frac{1}{m} e^{-mp} \right) \frac{d(1-d)}{n} \langle \sigma_{11}(t) \rangle \end{aligned} \quad (59)$$

When all variable evolution equations have been set, see eqs. from (52) to (59), this system of first order differential equations is solved using the non-linear ordinary differential equation solver ODE23, with pre-set options, from MATLAB® software.

4.3 Material parameters

Most of the basic material properties of the 316L(N)-IG austenitic stainless steel (see §2) can easily be found in the literature: density (ρ), lamé coefficient (λ and μ), mean thermal expansion coefficient (γ), material specific heat (C_ε), yield limit (σ_0) [11]. The following material parameters are applicable at ambient temperature:

- $\rho_0 = 7930 \text{ kg/m}^3$,
- $\gamma = 15.3 \cdot 10^{-6} \text{ K}^{-1}$,
- $C_\varepsilon = 472 \text{ J/kg.K}$,
- $\lambda = 115 \text{ 385 MPa}$ and $\mu = 76 \text{ 923 MPa}$,
- $\sigma_0 = 280 \text{ MPa}$.

The material parameters associated with the isotropic hardening (k , m), non-linear kinematic hardening (M_i , Γ_i), viscoplasticity (η , α) and damage parameters (n) were defined according to the mechanical test results described in §2.

The following material parameters are applicable at ambient temperature:

- $k = 220 \text{ MPa}$ and $m = 30$
- $M_1 = 400 \text{ MPa}$ and $\Gamma_1 = 10^3$,
- $M_2 = 15 \text{ MPa}$ and $\Gamma_2 = 0$,
- $\eta = 0.1 \text{ s}^{-1}$ and $\alpha = 1$,
- $n = 20 \text{ MPa}$.

It must be noted that the set of material parameters proposed here is not the only possible one. It was chosen by the physical interpretation of the mechanical test presented in §2 and is valid for similar loading conditions.

4.4 Results for monotonic loading

Fig. 18 represents the simulation in imposed stress with a rate of 35MPa/min (dashed blue line) and the one in imposed strain with a rate of 1 mm/mm (dashed red line), in accordance to the reference test (solid blue line) described in §2.1.

After point A, see Fig. 18, which corresponds to the yield of the so-called damage zone, the two curves are no

longer coincident. This phenomenon can be explained by the relation between the damage variable and the expression of the isotropic function described in eq.(22), in which the stress-strain evolution results from a competition between hardening and damage. In imposed strain simulation, when the damage zone is reached, the stress decreases down to zero, whereas in imposed stress simulation, the algorithm diverges in the damage zone.

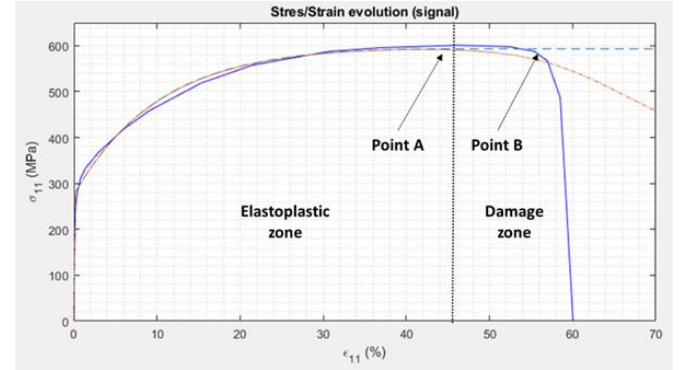


Fig. 18 – Stress/strain evolution

Fig. 19 shows the damage variable evolution, which is defined in eq. (35). By comparing this evolution to the stress tensor evolution from Fig. 18, we can observe that the damage variable remains close to zero up to 40% of strain. Beyond this value, the damage variable starts increasing, impacting the stress-strain evolution, see point A in the two figures. The value of $d=1$ is reached at 100% of strain, far from the ultimate strength observed during the experimental test, which occurs around 58% of strain, see point B in Fig. 18.

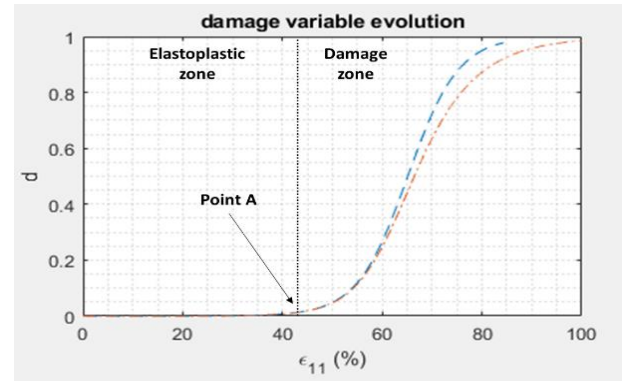


Fig. 19 – Damage variable evolution

When the damage variable is around 10^{-2} , see point A in Fig. 19, meaning that the collapse is imminent, the total strain evolution and that of the internal variables diverge. Beyond this critical point, the computed values of the different variables are physically meaningless.

To validate the temperature evolution, the mechanical test results presented in §2 should have been carried out under vacuum conditions, considering minimised radiation heat exchange with appropriate temperature monitoring. Due to this lack of experimental data, the temperature evolution curve presented in Fig. 20 cannot be superposed to any reference curve.

The heat equation as given by eq. (41), shows that the temperature evolution is dependent of the trace of the strain tensor evolution. In the elastic domain, where all the internal variables are equal to 0, a decrease of temperature is

observed, which is in agreement with classical results in thermoelasticity, see e.g. [26] . When the yield strength is reached, the temperature evolution depends on dissipation mechanisms (hardening and damage) which become higher than the thermoelastic mechanism and result in an increase in temperature.

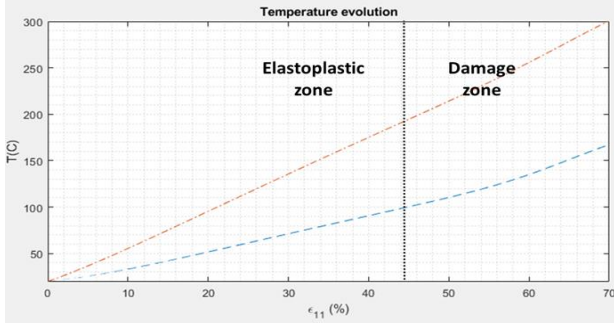


Fig. 20 – Temperature evolution

Note also that the strain rate difference for the two simulations, which is reported in Fig. 21, justifies the temperature evolution discrepancy between the two loading configuration.

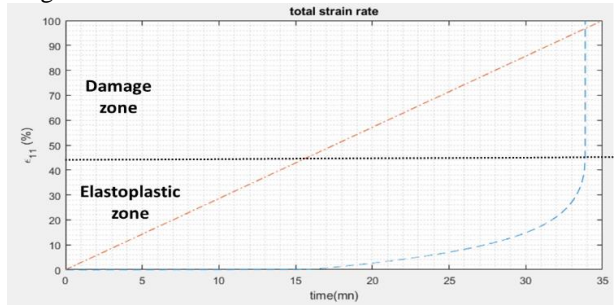


Fig. 21 – Comparison of total strain evolution between imposed stress & imposed strain simulations

4.5 Results for cyclic loading

For the cyclic simulations, the strong thermomechanical coupling have been removed, but the temperature evolution according to the heat equation has been conserved.

Fig. 22 shows the superposition of the reference engineering stress-strain curve (dashed line) obtained in the case of cyclic imposed force, see §2.2, Fig. 11, and the simulated stress-strain evolution curve in imposed stress assumption (solid line).

The simulated curve was obtained following the sinusoidal evolution described in eq.(2), where σ_{moy} is the mean stress, $\Delta\sigma$ is the stress range and $f=0.3\text{Hz}$ the frequency, and considering $\sigma_{max}=500\text{MPa}$ and $\sigma_{min}=-200\text{MPa}$.

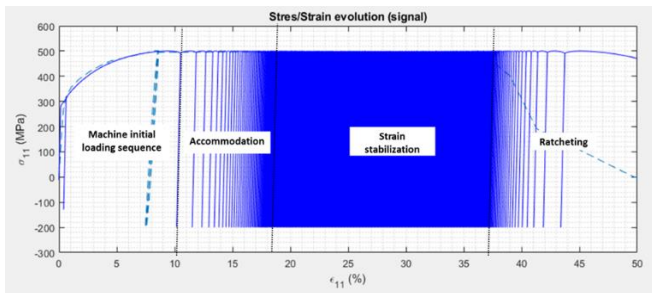


Fig. 22 – Stress/strain evolution

As in the experimental study, the first ten cycles correspond to the initial sequence which gradually reaches the nominal stress value, around 10% of strain. From this point up to 18% of deformation, an accommodation linked to the

isotropic hardening is observed. Then, from 18% up to 37% of deformation, the evolution of the strain is almost constant: in this zone, the isotropic hardening has reached its maximum value. The last part of the curve shows the ratcheting response up to the model divergence ($d=1$). Beyond this critical point, the computed values of the different variables are physically meaningless.

Fig. 23 gives the cumulated number of cycles with respect to the total strain evolution, where the blue dashed curve represents the 3574 cycles achieved during the reference test, and the dark blue one the simulated one. Although the chosen parameters allow to retrieve the same number of cycle, the simulated response has an offset of 10% in strain.

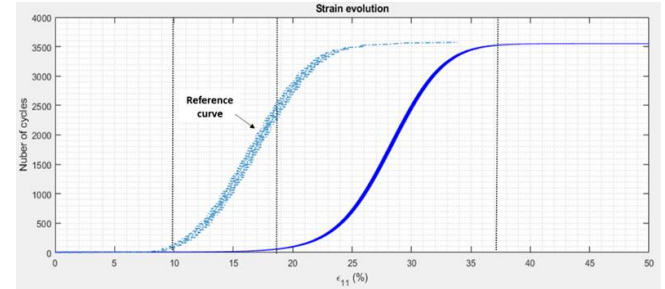


Fig. 23 – Total strain state relative to cumulative number of cycles

As it has been already observed for the monotonic simulation, when the damage evolution becomes fast, the ratcheting phenomenon is triggered. In Fig. 23, the total number of cycles stops growing at 35% of total strain, which corresponds to the change of slope for the damage variable, see Fig. 24. Contrary to what was expected, the algorithm diverges at value of d around 0.02, far from maximum admissible value ($d=1$).

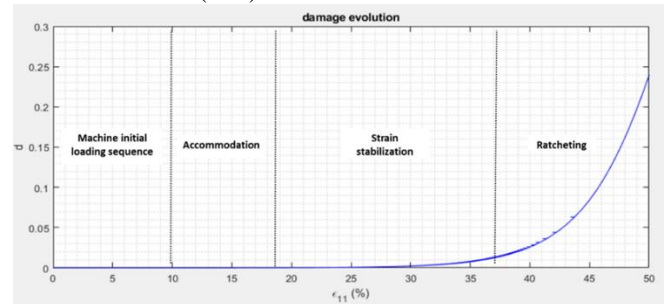


Fig. 24 – Damage variable evolution

Fig. 25 shows the temperature evolution linked to the mechanical behavior via eq.(59). The adiabatic hypothesis underlying the simulations does not allow any thermal dissipation, resulting in an unrealistic temperature range.

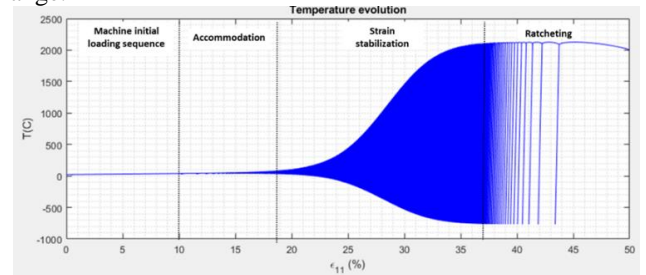


Fig. 25 – Temperature evolution

Finally, the input signal has been modified by $\pm 60\text{MPa}$. The results are reported in Fig. 26 and Fig. 27. Compared to the reference simulation where $\Delta\sigma=700\text{MPa}$ (blue curve), a decrease in the signal amplitude (pink curve) increases the

number of cycles and reduces the total strain while an amplitude increase of the signal (red curve) induces the opposite response. From these three simulations it can be observed an elastic shakedown (small stress amplitude), a strain evolution up to ratcheting (reference signal) and a pure ratcheting response (high stress amplitude signal). Thus, the model demonstrates its ability to account for different phenomena, such as shakedown and ratcheting, depending on the stress intensity.

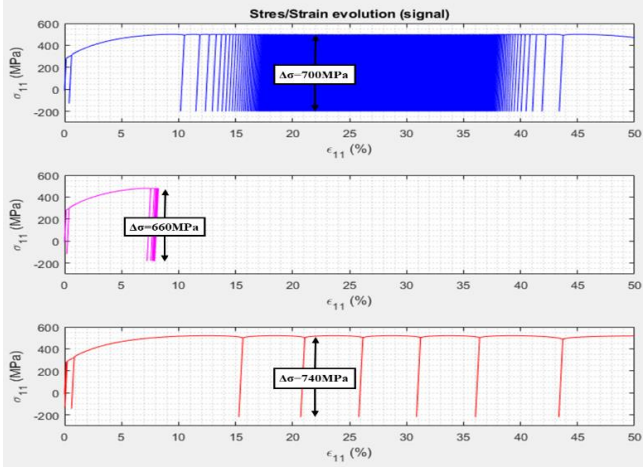


Fig. 26 – Model predictions: comparison for different input signals

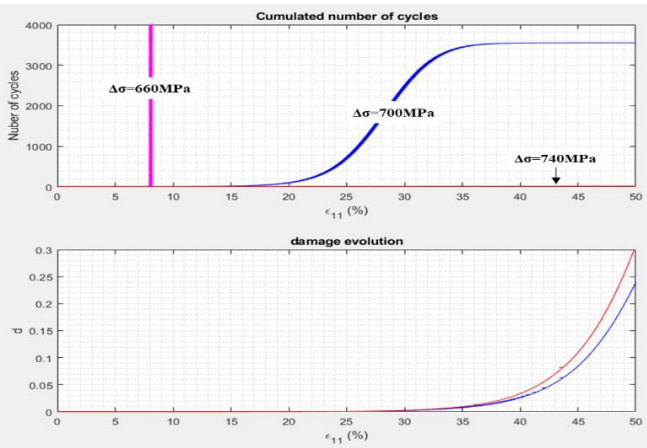


Fig. 27 – Model predictions: comparison for different input signals

The results presented in this paragraph show that the proposed model is able to reproduce all the mechanical phenomena that have been experimentally observed, see §2. More complex cases (structural problems) require the implementation of the constitutive model into the finite element software.

5 Numerical implementation

In the following, we adopt a fully coupled thermomechanical formulation of the problem. The finite element implementation was done in Abaqus® with the help of UMAT and UMATHT subroutines.

5.1 Abaqus implementation of strong thermo-mechanical couplings

For a better understanding, we recall here the formulation that is implemented in Abaqus for the case of strong and transient thermomechanical couplings. If one consider a closed domain, Ω , which is stress free in the initial configuration at the initial temperature, T_0 . Mechanical boundary conditions apply onto $\partial\Omega_u$ for displacements and

$\partial\Omega_\sigma$ for forces. Thermal boundary conditions apply onto $\partial\Omega_T$ for temperature and $\partial\Omega_q$ for thermal flux. The weak formulation of the thermomechanical problem, at small strain, is:

$$\text{Find } (\mathbf{u}, T) \text{ such that } \forall (\delta \mathbf{u}, \delta T): \left\{ \begin{array}{l} \int_{\Omega} \boldsymbol{\sigma} : (\mathbf{grad}(\delta \mathbf{u}))_{sym} d\Omega - \int_{\partial\Omega_\sigma} (\boldsymbol{\sigma} \cdot \mathbf{n}) \cdot \delta \mathbf{u} ds \\ - \int_{\Omega} \mathbf{f}^v \cdot \delta \mathbf{u} d\Omega = 0 \\ \int_{\Omega} \left(\frac{\rho_0 C_\epsilon}{T_0} T \dot{T} \delta T - T \left(\frac{\partial \boldsymbol{\sigma}}{\partial T} : \dot{\boldsymbol{\epsilon}} \right) \delta T - \varnothing_{int} \delta T - r^v \delta T \right) d\Omega \\ - \int_{\partial\Omega_q} \mathbf{q}^s \cdot \mathbf{n} \delta T ds = 0 \end{array} \right. \quad (60)$$

where \mathbf{q}^s is the prescribed flux on the surface $\partial\Omega_q$. Abaqus uses a backward-difference scheme that consists in the following approximations: $\dot{T} = (T(t_{n+1}) - T(t_n))/\Delta t$ and $\dot{\mathbf{u}} = (\mathbf{u}(t_{n+1}) - \mathbf{u}(t_n))/\Delta t$. For the sake of simplicity, we note all quantities at time t_{n+1} without indexes and we note T_n the temperature at time t_n (same notation for \mathbf{u}). Therefore, the time discretisation of the system eq. (60) is:

On a time interval $[t_n, t_{n+1}]$, find (\mathbf{u}, T) knowing (\mathbf{u}_n, T_n) such that $\forall (\delta \mathbf{u}, \delta T)$:

$$\left\{ \begin{array}{l} \int_{\Omega} \boldsymbol{\sigma} : (\mathbf{grad}(\delta \mathbf{u}))_{sym} d\Omega - \int_{\partial\Omega_\sigma} (\boldsymbol{\sigma} \cdot \mathbf{n}) \cdot \delta \mathbf{u} ds \\ - \int_{\Omega} \mathbf{f}^v \cdot \delta \mathbf{u} d\Omega = 0 \\ \int_{\Omega} \left(\frac{\rho_0 C_\epsilon}{T_0} T \frac{(T - T_n)}{\Delta t} \delta T - T \left(\frac{\partial \boldsymbol{\sigma}}{\partial T} : \frac{(\boldsymbol{\epsilon} - \boldsymbol{\epsilon}_n)}{\Delta t} \right) \delta T \right) d\Omega \\ - r^v \delta T - \varnothing_{int} \delta T - \int_{\partial\Omega_q} \mathbf{q}^s \cdot \mathbf{n} \delta T ds = 0 \end{array} \right. \quad (61)$$

In the UMAT subroutine we need to implement the computation of $\boldsymbol{\sigma}$, \varnothing_{int} and $\partial\boldsymbol{\sigma}/\partial\Delta T$ (in Abaqus an incremental formulation of eqs.(61) is used). Furthermore we also need to define the consistent jacobian, $\partial\boldsymbol{\sigma}/\partial\Delta\boldsymbol{\epsilon}$, and the variation of the dissipation relative to the temperature $\partial\varnothing_{int}/\partial T$ that comes from the linearization of the incremental form of eqs.(61). In the UMATHT subroutine we have to implement the thermal part of the internal energy, denoted by U in the Abaqus documentation, and its derivative upon temperature. By identifying thermal internal energy from eqs.(61), one can find: $U = C_\epsilon(T/T_0)T$ and $\partial U/\partial T = 2C_\epsilon(T/T_0)$. The thermal expansion part of the stress can be taken into account with the expansion material property that can be defined independently of UMAT and UMATHT subroutine. In this case the strain passed as argument in UMAT is only the mechanical strain (expansion contribution is previously removed).

5.2 Local integration of internal variables

The previous finite element formulation requires to evaluate the mechanical stresses at time t_{n+1} at the Gauss point level on each element. Therefore, we need to integrate the evolution of the internal variables during the time interval knowing their values at a previous time increment and having a prediction of the current strain value $\boldsymbol{\epsilon}_{n+1}$ and the current temperature T_{n+1} locally at each Gauss point. In this work, we adopt the return mapping approach as earlier proposed by Simo [27] and used later by several authors (see for instance [28] and [29]). A global flow chart of this approach is given in Fig. 28.

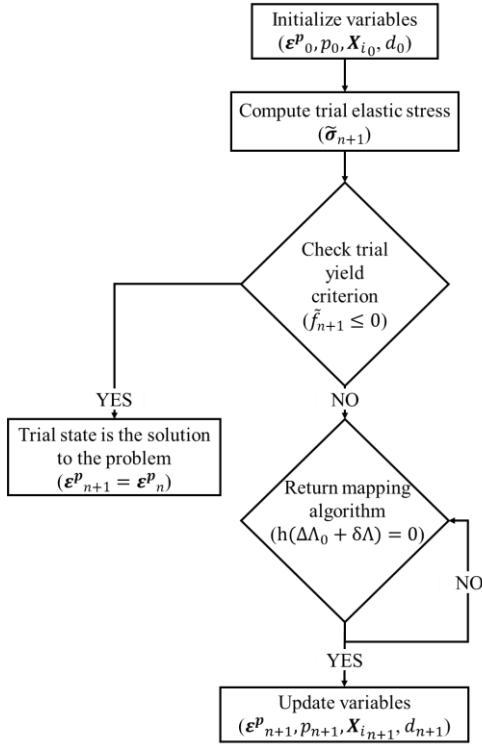


Fig. 28 – Flow chart for the return-mapping algorithm [27]

The return mapping algorithm is based on the definition of a trial state for which the plastic flow (and kinematic hardening) is frozen. We therefore assume that the trial state at time t_{n+1} , is equal to the last converged value, so that:

$$\tilde{\boldsymbol{\varepsilon}}^p_{n+1} = \boldsymbol{\varepsilon}^p_n, \tilde{p}_{n+1} = p_n, \tilde{d}_{n+1} = d_n, \tilde{\mathbf{X}}_{(i)n+1} = \mathbf{X}_{(i)n} \quad \forall i \quad (62)$$

We can therefore define a trial stress tensor $\tilde{\boldsymbol{\sigma}}_{n+1}$, eq.(63) and a trial yield function \tilde{f}_{n+1} , eq.(64) such that:

$$\tilde{\boldsymbol{\sigma}}_{n+1} = \lambda \text{Tr}(\boldsymbol{\varepsilon}_{n+1} - \boldsymbol{\varepsilon}^p_n) \mathbf{G} + 2\mu(\boldsymbol{\varepsilon}_{n+1} - \boldsymbol{\varepsilon}^p_n) - (3\lambda + 2\mu)\gamma(T_{n+1} - T_0) \mathbf{G} \quad (63)$$

$$\tilde{f}_{n+1} = \sqrt{\frac{3}{2}} \left\| \text{Dev} \left(\tilde{\boldsymbol{\sigma}}_{n+1} - \sum_{i=1}^{N_{kh}} M_i \mathbf{X}_{(i)n} \right) \right\| - \sigma_0 - A^p_n \quad (64)$$

If the trial yield criterion is satisfied ($\tilde{f}_{n+1} \leq 0$), this means that the trial state is admissible, inducing an elastic deformation. In that case, the expression of $\boldsymbol{\sigma}_{n+1}$ can be explicitly computed and we have:

$$\boldsymbol{\varepsilon}^p_{n+1} = \boldsymbol{\varepsilon}^p_n \quad (65)$$

$$p_{n+1} = p_n \quad (66)$$

$$\mathbf{X}_{(i)n+1} = \mathbf{X}_{(i)n} \quad \forall i \quad (67)$$

$$d_{n+1} = d_n \quad (68)$$

If the trial yield criterion is not satisfied ($\tilde{f}_{n+1} > 0$), we need to integrate the evolution of the internal variables on the time interval. We first assume a backward Euler expression of the plastic strain flow in eq. (32):

$$\boldsymbol{\varepsilon}^p_{n+1} - \boldsymbol{\varepsilon}^p_n = \sqrt{\frac{3}{2}} \mathbf{n}_{n+1} \Delta\Lambda \quad (69)$$

where the plastic flow direction, \mathbf{n}_{n+1} , is defined by:

$$\mathbf{n}_{n+1} = \frac{\mathbf{S}_{n+1}}{\|\mathbf{S}_{n+1}\|} \quad (70)$$

with \mathbf{S}_{n+1} , is defined by:

$$\mathbf{S}_{n+1} = \text{Dev} \left(\boldsymbol{\sigma}_{n+1} - \sum_{i=1}^{N_{kh}} M_i \mathbf{X}_{(i)n+1} \right) \quad (71)$$

and

$$\Delta\Lambda = \Lambda_{n+1}(t_{n+1} - t_n) = \Delta t \frac{1}{\eta \sigma_0} \langle f_{n+1} \rangle \quad (72)$$

Following the same methodology, the expression of the evolution of the other variables $\dot{\mathbf{X}}$, \dot{p} and \dot{d} , see eq.(33), eq.(34) and eq.(35), appears as:

$$\mathbf{X}_{(i)n+1} - \mathbf{X}_{(i)n} = \Delta\Lambda \left(\sqrt{\frac{3}{2}} \mathbf{n}_{n+1} - d_{n+1} \Gamma_i \mathbf{X}_{(i)n+1} \right) \quad (73)$$

$$p_{n+1} - p_n = \Delta\Lambda \quad (74)$$

$$d_{n+1} - d_n = \Delta\Lambda \frac{d_{n+1}(1 - d_{n+1})}{n} \langle \text{Tr}(\boldsymbol{\sigma}_{n+1}) \rangle \quad (75)$$

From eq. (63) and using eq. (69), one can obtain:

$$\text{Dev}(\boldsymbol{\sigma}_{n+1}) = \text{Dev}(\tilde{\boldsymbol{\sigma}}_{n+1}) - 2\mu \text{Dev}(\boldsymbol{\varepsilon}^p_{n+1} - \boldsymbol{\varepsilon}^p_n) \quad (76)$$

rewriting eq. (73), so that:

$$\mathbf{X}_{(i)n+1} = \left(\sqrt{\frac{3}{2}} \mathbf{n}_{n+1} \Delta\Lambda + \mathbf{X}_{(i)n} \right) \delta_{(i)n+1} \quad (77)$$

with:

$$\delta_{(i)n+1} = \frac{1}{(1 + d_{n+1} \Gamma_i \Delta\Lambda)} \quad (78)$$

Using eqs.(71) (76) (77), one can obtain:

$$\begin{aligned} & \text{Dev} \left(\boldsymbol{\sigma}_{n+1} - d_{n+1} \sum_{i=1}^{N_{kh}} M_i \mathbf{X}_{(i)n+1} \right) \\ & \left(1 + \frac{\xi_{(i)n+1}}{\|\text{Dev}(\boldsymbol{\sigma}_{n+1} - d_{n+1} \sum_{i=1}^{N_{kh}} M_i \mathbf{X}_{(i)n+1})\|} \right) = \\ & \text{Dev} \left(\tilde{\boldsymbol{\sigma}}_{n+1} - d_{n+1} \sum_{i=1}^{N_{kh}} M_i \delta_{(i)n+1} \mathbf{X}_{(i)n} \right) \end{aligned} \quad (79)$$

where :

$$\xi_{(i)n+1} = \left(2\mu + d_{n+1} \sum_{i=1}^{N_{kh}} M_i \delta_{(i)n+1} \right) \sqrt{\frac{3}{2}} \Delta\Lambda \quad (80)$$

Taking the norm of eq. (79) and using the fact that $\xi_{(i)n+1}$ is strictly positive, we can obtain the following relation:

$$\begin{aligned} & \left\| \text{Dev} \left(\boldsymbol{\sigma}_{n+1} - d_{n+1} \sum_{i=1}^{N_{kh}} M_i \mathbf{X}_{(i)n+1} \right) \right\| = \\ & \left\| \text{Dev} \left(\tilde{\boldsymbol{\sigma}}_{n+1} - d_{n+1} \sum_{i=1}^{N_{kh}} M_i \delta_{(i)n+1} \mathbf{X}_{(i)n} \right) \right\| - \xi_{(i)n+1} \end{aligned} \quad (81)$$

From eq. (79) and (81) we can deduce that:

$$\begin{aligned} & \mathbf{n}_{n+1} \\ & = \frac{\text{Dev}(\tilde{\boldsymbol{\sigma}}_{n+1} - d_{n+1} \sum_{i=1}^{N_{kh}} M_i \delta_{(i)n+1} \mathbf{X}_{(i)n})}{\|\text{Dev}(\tilde{\boldsymbol{\sigma}}_{n+1} - d_{n+1} \sum_{i=1}^{N_{kh}} M_i \delta_{(i)n+1} \mathbf{X}_{(i)n})\|} \end{aligned} \quad (82)$$

To compute the direction of plastic flow, \mathbf{n}_{n+1} , we need to determine the plastic multiplier increment and the current damage value. From eq. (37) and eq. (75) we obtain the following nonlinear system of equations:

$$\begin{cases} \sqrt{\frac{3}{2}} \left(\left\| \text{Dev} \left(\tilde{\sigma}_{n+1} - d_{n+1} \sum_{i=1}^{N_{kh}} M_i \delta_{(i)n+1} \mathbf{X}_{(i)n} \right) \right\| - \xi_{(i)n+1} \right) \\ -A^p_{n+1} - \sigma_0 - \eta \left(\frac{\Delta \Lambda}{\Delta t} \sigma_0 \right)^{\frac{1}{\alpha}} = 0 \\ d_{n+1} - d_n - \Delta \Lambda \frac{d_{n+1}(1-d_{n+1})}{n} \langle \text{Tr}(\tilde{\sigma}_{n+1}) \rangle = 0 \end{cases} \quad (83)$$

with :

$$\text{Tr}(\sigma_{n+1}) = (3\lambda + 2\mu) \text{Tr}(\varepsilon_{n+1}) + 3(3\lambda + 2\mu) \gamma (T_{n+1} - T_0) \quad (85)$$

$$A^p_{n+1} = k(d_{n+1} - 1) \left(1 - e^{-m(\Delta \Lambda + p_n)} \right) \quad (86)$$

The system of eqs.(83)-(84) depends only on $\Delta \Lambda, d_{n+1}$ as $\varepsilon_{n+1}, T_{n+1}$ are given from the global Newton-Raphson scheme (predictor values) and every other quantity is known from the last converged increment. The previous non-linear system can be linearised and solved with a local (at Gauss point level) Newton scheme. This algorithm and the local Newton scheme is implemented in the UMAT subroutine.

Once $\Delta \Lambda, d_{n+1}$ are known, we can evaluate the plastic flow direction, \mathbf{n}_{n+1} from eq. (82) and the evolution of kinetic tensors $\mathbf{X}_{(i)n+1}$ and plastic strain from eqs. (73) and (69).

6 Application to ITER Vacuum Vessel (VV) support rail

The VV interfaces with various systems of the machine through a bolted connection onto a supporting ‘‘rail’’ welded to the confinement barrier. Fig. 29 shows the manifold rails of the blanket system in the ITER vacuum vessel. The design justification for these rails consists in evaluating the maximum stress and/or strain in the weld cross section for the worst load combination [4], and comparing it with design criteria defined in the RCC-MR code.

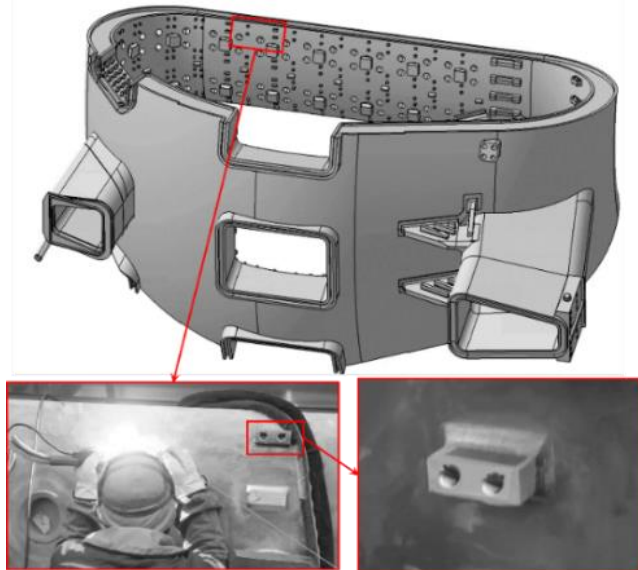


Fig. 29 – ITER VV rails [30].

6.1 Thermomechanical test hypothesis

Because of the large amount of rails in the VV and all the different mechanical load types that could act on it, the method proposed here consists in redefining the loading vector applied at the centroid of the weld cross section A (in m^2) in two forces: one normal force $F_n(t)$ (in N) and one tangential force $F_t(t)$ (in N), see eq.(87)-(88)-(89).

$$F_n = F_z + \frac{e \cdot A}{2 \cdot I_y} \cdot M_y + \frac{h \cdot A}{2 \cdot I_x} \cdot M_x \quad (87)$$

$$F_t = \sqrt{(F_x^2 + F_y^2)} + F_{torque} \quad (88)$$

$$F_{torque} = \frac{3 \cdot M_z}{8 \cdot w \cdot e^2} \cdot A \cdot \left(1 + 0.6095 \cdot \frac{w}{e} + 0.8865 \cdot \left(\frac{w}{e} \right)^2 - 1.8023 \cdot \left(\frac{w}{e} \right)^3 + 0.9100 \cdot \left(\frac{w}{e} \right)^4 \right) \quad (89)$$

where F_x, F_y, F_z are the forces, and M_x, M_y, M_z are the moments (in N.m) defined in a given orthonormal basis ($\mathbf{x}, \mathbf{y}, \mathbf{z}$), and e corresponds to the rail thickness (in m), w the rail width (in m), I_x and I_y are the flexion moments of inertia (in m^4). The force induced by torsion in a rectangular section, F_{torque} (N), has been adapted from [31].

From a thermal point of view, the power deposition onto the rail is a combination of nuclear heating, conduction and radiation with the surrounding components. To simplify this combination of heat depositions, it is proposed to model it as an imposed temperature gradient in the rail, where the VV shell temperature is fixed at 373K and the maximum temperature, defined by $g(t)$, is applied on top of the rails, see Fig. 30.

The geometry has also been simplified by neglecting the radius of curvature of the VV and removing the weld fillet at the junction of the rail. We have therefore 2 rectangular blocks with a perfect interface. Symmetry conditions are applied on the largest rectangular block (dark blue in Fig. 30) and vertical displacement are prescribed to be null on its top edges (light blue in Fig. 30).

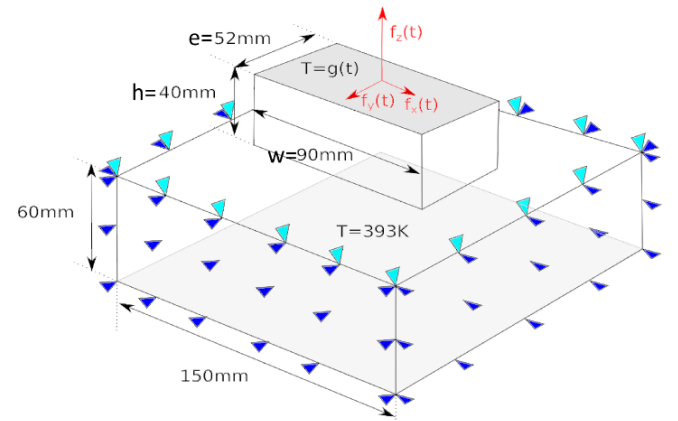


Fig. 30 – Welded interface between VV (blue) and rail (green)

Finally, the same material parameters than the one proposed in §4.3 have been used.

6.2 Results for monotonic loading

In the first numerical simulation, a ramped thermal load (see Fig. 31) is combined with a piecewise linear, mechanical load (see Fig. 32). The values proposed here are not realistic. They aim at reaching the damage mode to test the proposed model.

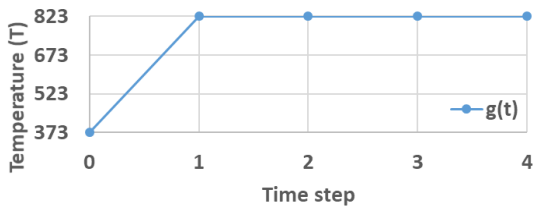


Fig. 31 – Applied input temperature for monotonic simulation

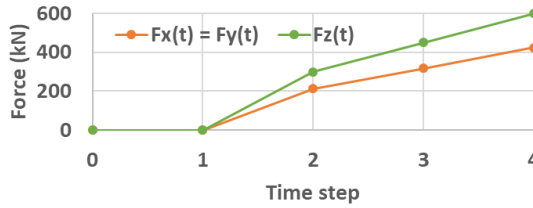


Fig. 32 – Applied input forces for monotonic simulation

Fig. 33 shows the maximum principal strain map distribution at the end of step-03. It can be observed that the rail bends under the combination of loads, which localizes the strain in the two opposite corners; one is subjected to compression and the second to tension.

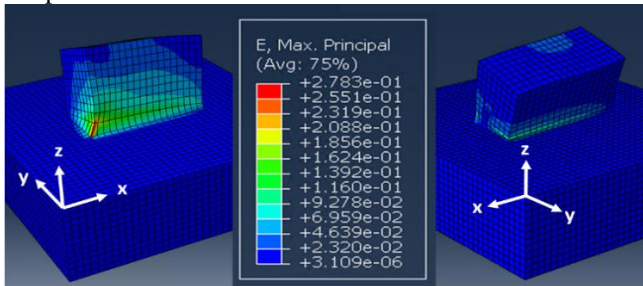


Fig. 33 – Maximum principal strain map at the end of step-03 (monotonic simulation)

Fig. 34 shows the damage map distribution at the end of step-03. Although the strain is localized in the two corners, the damage occurs only in the tension area. This material response corresponds to the damage evolution defined in eq.(35), which supposes that the microcrack propagation and the growth of cavities depends on the tensile loading only.

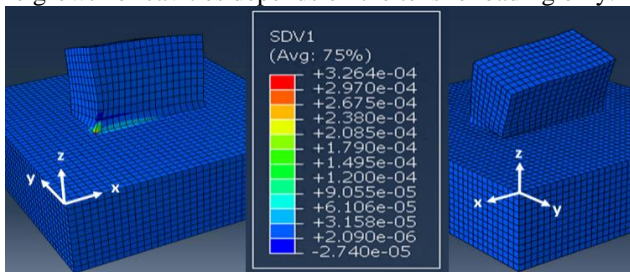


Fig. 34 – Damage map at the end of step-03 (monotonic simulation)

Fig. 35 shows the damage evolution in a Gauss point of the corner element where the strain is maximum. Similarly to what was observed for “0D”simulation, see §4.4, the damage variable starts increasing exponentially between step-02 and step-03, which corresponds to a total strain value between 10% and 20%, see the total strain evolution in the same Gauss point in Fig. 36. We can notice that the rapid damage

evolution leads to the divergence of the algorithm before reaching step-04.

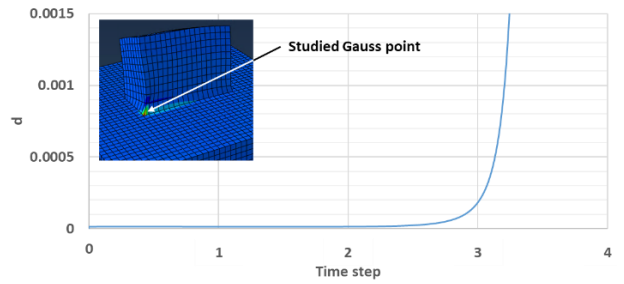


Fig. 35 – Damage evolution for monotonic simulation

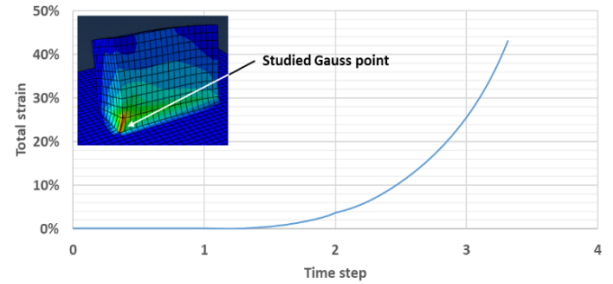


Fig. 36 – Total strain evolution for monotonic simulation

6.3 Results for cyclic loading

For the second simulation, we propose to start from the end of step-03 of the monotonic simulation, where the damage variable start to grow. From this step, the mechanical load is kept at a constant value, and the thermal load is cycled 20 times, see Fig. 31 and Fig. 32.

For this scenario where the primary load is fixed and the secondary load is cycled, the goal is to check if the material response will lead to shakedown or ratcheting.

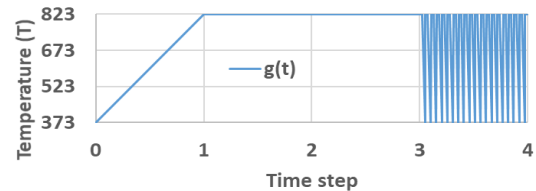


Fig. 37 – Applied input temperature for cyclic simulation

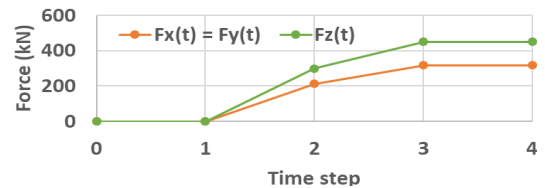


Fig. 38 – Applied input forces for cyclic simulation

Fig. 39 shows the maximum principal strain map distribution at the end of step-04. A similar behavior as in the monotonic loading case is observed, where the strain mainly localizes in the two opposite corners.

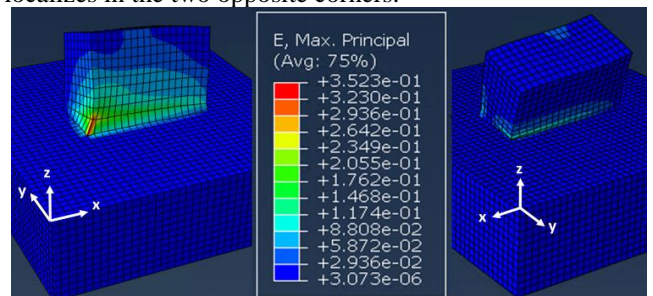


Fig. 39 – Maximum principal strain map at the end of step-04 (cyclic simulation)

Fig. 40 shows the damage map at the end of step-04. In comparison to the monotonic loading case, the damage still occurs in the same corner. Moreover, even if the damage variable increases on the loaded corner under cyclic thermal load, it remains close to its initial value in the opposite corner.

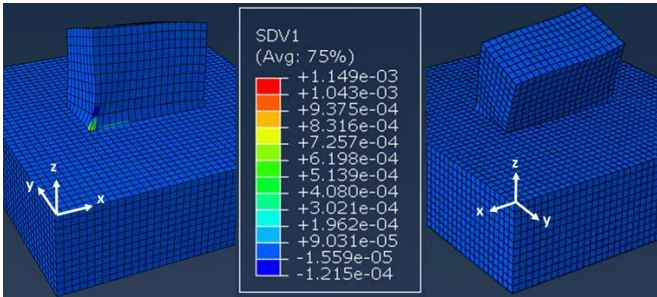


Fig. 40 – Damage map at the end of step-04 (cyclic simulation)

Fig. 41 shows the damage evolution in a Gauss point of the corner element where the strain is maximum. At the end of step-03, when the primary load is fixed and the cyclic secondary load starts, we can observe a change in the damage evolution. Effectively, the exponential trend has changed to a logarithmic one, which corresponds to an accommodation of the material. It should be noted that this evolution is strongly localized and we have not studied the influence of the mesh size on it.

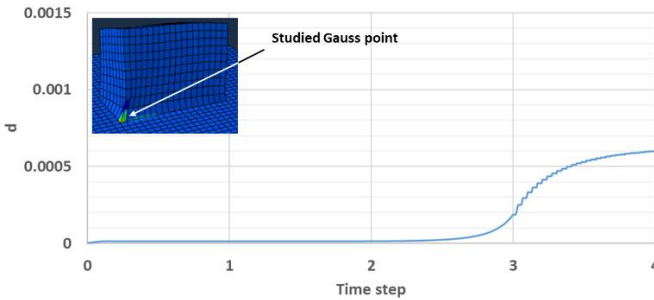


Fig. 41 – Damage evolution for cyclic simulation

Finally, Fig. 42, which shows the total strain evolution in a Gauss point of the corner element, confirms that a shakedown occurs under thermal cyclic loads.

This observation allows us to conclude that the failure mode could be due to high-cycle fatigue rather than to ratcheting.

However, the present model is limited to shakedown justification. Further analysis following the RCC-MR code methodology, which is more adapted for fatigue justification, would be required to confirm the observed behaviour.

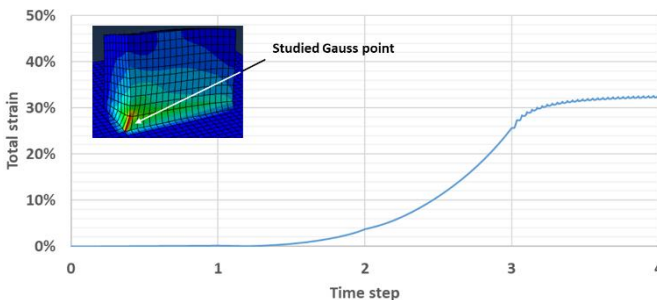


Fig. 42 – Total strain evolution for cyclic simulation

7 Conclusions

The present paper highlights the material behaviour of the 316L(N)-IG austenitic stainless steel used for the first confinement barrier of the ITER fusion thermonuclear reactor. One of the most complex phenomena under cyclic loading conditions remains the ratcheting phenomenon, which occurs during oligocyclic fatigue.

Based on a phenomenological approach, the study consisted in enriching an elasto-visco-plastic model including both isotropic and kinematic hardening variables with strong thermo-mechanical coupling and damage variable.

The results of cyclic tension/compression tests conducted in imposed stress show that the material undergoes elastic shakedown at low stress amplitude and plastic shakedown up to ratcheting at higher stress amplitude. That is why in the proposed model, we implemented a damage variable in both kinematic and isotropic hardening behaviours. The objective was to have the two hardening modes working in opposition, meaning that in the low damage state the isotropic hardening is dominant whereas in a higher damage state, the kinematic hardening becomes dominant. Ratcheting occurs in the final stage, only if the damage variable evolution progresses significantly up to the value over 10^{-2} .

The different phenomena highlighted above were first demonstrated through “0D analysis” using MATLAB® software. This simplistic approach makes it possible to choose appropriate parameters, which most of the time requires complex methodologies.

Finally, this model was implemented in an in-house code specially designed to facilitate multi-field and multi-physics formulation developments. A finite element geometry representative of the ITER Vacuum Vessel structure was tested under different load conditions demonstrating the proper behaviour of the model under strong thermomechanical coupling in 3D environment.

It is important to note that this paper initiates a work, which needs to be consolidated with more experimental data, since the test campaign used to identify the material parameters was done only at 20°C for uniaxial loading. It can be complemented by performing combined loading tests (like torsion/compression) for different temperature environments. To validate the temperature evolution, some tests should be done under vacuum conditions, considering a minimised radiation heat exchange.

8 Future perspectives

The ITER plasma-facing components and vacuum chamber will be exposed to highly energetic neutron fluxes in the order of 14 MeV, generated during the Deuterium-Tritium fusion reaction. These neutron structure interactions will produce various types of secondary reactions, from which gamma rays and/or charged particles will be created. The neutrons and photons, which are by definition electrically neutral, cross the magnetic confinement and penetrate deeply into the structural parts, converting their kinetic energy into thermal energy [32].

Based on this statement, the analysis software used in ITER for volume heating evaluation takes into account two contributors, which are the neutron and photon heating sources. Fig. 43 shows an example of what a map of nuclear heating distribution on the ITER vacuum vessel can be.

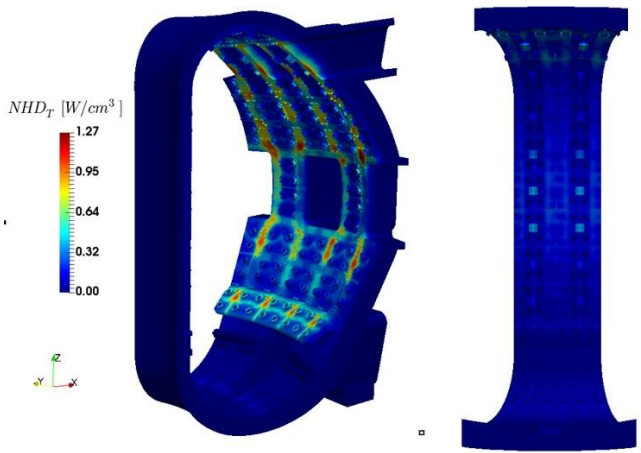


Fig. 43 – ITER VV nuclear heating distribution map [33].

In addition to the heat power exchange, the neutron kinetic energy is so high that it allows atoms to move from their site. This results in a local displacement chain, limited in time and space, which modifies the crystalline structure of the material. Fig. 44 shows a schematic representation of the displacement cascade induced after a Primary Knocked-on Atoms (PKA). This phenomenon is quantified in displacement per atoms (dpa). This means that for a material receiving a dose of 100 dpa, each atom moves 100 times [34].

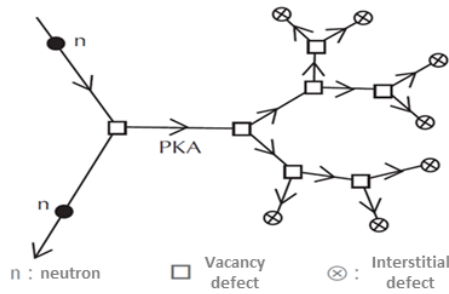


Fig. 44 – Displacement cascade scheme [34]

During the initial collision between neutron and atom (PKA), nuclear transmutation reactions occur. In nuclear fusion reactors, the worst reaction, which is the most sensitive for material damage, generates helium and hydrogen atoms. This atoms generation is made inside the steel structure with a rate of ~ 12 appmHe/dpa ($12 \cdot 10^{-6}$ atoms per dpa) for helium and ~ 45 appmH/dpa for hydrogen.

For ITER In Vessel components, which operate at temperature condition set as a maximum of 450°C (below the thermal creep for steel material), the expected neutron fluence is about $0.3\text{MWa}/\text{m}^2$ where the peak damage in the steel would be about 2 dpa with a maximum helium generation of 55appm [35].

The irradiation affects the physical properties through generations of dpa and nuclear transmutation that can be divided in two cases. The first covers various mechanical coefficients like the yield strength, electrical resistivity and magnetic permeability, and the second covers density and Young modulus.

For austenitic stainless steel, this damage results in an increase in the yield limit and a reduction in the plastic flow area. Fig. 46 shows the design curves for the minimum yield strength of 316L (N)-IG steel as a function of neutron damage at a temperature range of $100\text{--}300^\circ\text{C}$ as well as the minimum uniform elongation for different doses [10].

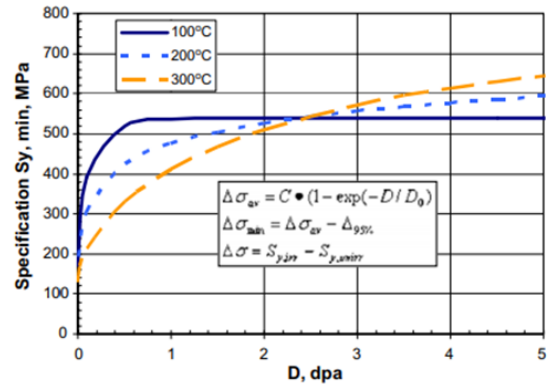


Fig. 45 – Neutron irradiation effect on minimum yield strength (σ_0) of 316L(N)-IG steel [10].

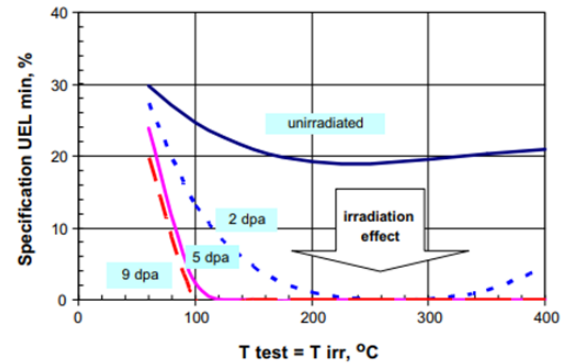


Fig. 46 – Neutron irradiation effect on minimum elongation (UE) of 316L(N)-IG steel [10].

The swelling corresponds to a volume increase due to the accumulation of cavities and vacancies induced by neutron damage. Fig. 47 shows the volume evolution between the initial coupon of CW 316 steel and the same coupon after irradiation up to 15 dpa at 533°C [36]. It is important to note that this phenomenon is amplified at certain temperature range, generally close to the thermal creep temperature, see Fig. 48. This swelling phenomenon can have an effect on the Young modulus when large quantities of helium are formed due to the material effective cross section reduction.

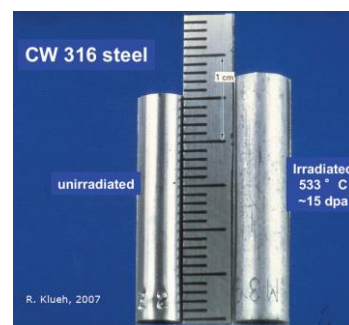


Fig. 47 – Swelling (effect of vacancy clustering) of CW 316 steel [36].

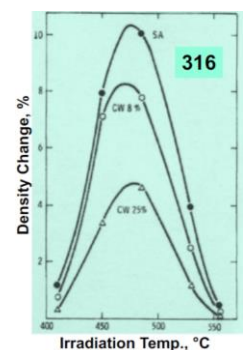


Fig. 48 – Density evolution of CW 316 steel vs environment temperature [36].

Furthering the work presented in this paper would be to enrich the thermo-mechanical model by including a second damage variable. This new variable would be associated with the neutron flux that drives the dpa and a part of the nuclear heating (τ^v in eq.(41)). This updated model would reinforce the interest of using a strong thermo-mechanic coupling approach.

ITER Disclaimer

The views and opinions expressed herein do not necessarily reflect those of the ITER Organization.

Acknowledgments

The authors acknowledge the support of members of IO-CT who have worked conjointly as Vacuum Vessel Project Team and the LMA members for the various activities reported in this paper.

References

- [1] F. Sabourin, "Application of 3D View Factor method for heat fluxes deposition on ITER Cryostat Thermal Shield," *Fusion Engineering and design*, 2018.
- [2] J.-M. Martinez, "Structural analysis of the ITER Vacuum Vessel regarding 2012 ITER Project-Level Loads," *Fusion Engineering and Design*, vol. 89, pp. 1836-1842, 2014.
- [3] AFCEN, RCC-MR -Regles de Conception et de Construction des materiels mecaniques des installations nucleaires-, 2007.
- [4] J.-M. Martinez, "ITER vacuum vessel structural analysis completion during manufacturing phase," *Fusion Engineering and Design*, Vols. 109-111, pp. 688-692, 2016.
- [5] J.-M. Martinez, "Structural damages prevention of the ITER vacuum vessel and ports by elasto-plastic analysis with regards to RCC-MR," *Fusion Engineering and Design*, Vols. 98-99, pp. 1552-1555, 2015.
- [6] H. Hübel, "Basic conditions for material and structural ratcheting," *Nuclear Engineering and Design*, vol. 162, no. 1, pp. 55-65, 1996.
- [7] J.-L. Chaboche and J. Lemaitre, *Mechanics of solid materials*, second ed., France: Dunod, 1988.
- [8] M. Kobayashi and N. Ohno, "Thermal ratcheting of a cylinder subjected to a moving temperature front: Effects of kinematic hardening rules on the analysis," *International Journal of Plasticity*, vol. 12, no. 2, pp. 255-271, 1996.
- [9] J. Bree, "Elastic-plastic behaviour of thin tubes subjected to internal pressure and intermittent high-heat fluxes with application to fast-nuclear-reactor fuel elements," *The Journal of Strain Analysis for Engineering Design*, vol. 2, no. 3, 1967.
- [10] V. Barabash, "Materials challenges for ITER - Current status and future activities -," *Journal of Nuclear Materials*, Vols. 367-370, pp. 21-32, 2007.
- [11] G. Kalinin, "Structural materials for ITER in-vessel component design," *Journal of Nuclear Materials*, Vols. 233-237, pp. 9-16, 1996.
- [12] B. Coleman and M. Gurtin, "Thermodynamics with Internal State Variables," *The Journal of Chemical Physics*, vol. 47.2, pp. 597-613, 1967.
- [13] D. Nouailhas, "Modélisation de l'écroutissage et de la restauration en viscoplasticité cyclique," *Revue Phys. Appl.*, vol. 23, pp. 339-349, 1988.
- [14] G. Rousselier, "Ductile fracture models and their potential," *Nuclear Engineering and Design*, vol. 105, pp. 97-111, 1987.
- [15] J. Lemaitre, "Coupled elasto-viscoplasticity and damage constitute equations," *Computer methods in applied mechanics and engineering*, vol. 51, pp. 31-49, 1985.
- [16] P. Germain, P. Suquet and Q. Nguyen, "Continuum Thermodynamics," *Journal of Applied Mechanics, American Society of Mechanical Engineers (ASME)*, vol. 50, pp. 1010-1020, 1983.
- [17] P.-J. Armstrong and C.-O. Frederick, "A mathematical representation of the multiaxial Bauschinger effect," Central Electricity Generating Board & Berkeley Nuclear Laboratories, 1966.
- [18] J.-L. Chaboche, "On some modifications of kinematic hardening to improve the description of ratchetting effects," *International Journal of Plasticity*, vol. 7, no. 7, pp. 661-678, 1991.
- [19] N. Ohno and J.-D. Wang, "Kinematic hardening rules with critical state of dynamic recovery, part I: formulation and basic features for ratchetting behavior," *International Journal of Plasticity*, vol. 9, pp. 375-390, 1993.
- [20] N. Ohno and J.-D. Wang, "Kinematic hardening rules with critical state of dynamic recovery, part II: application to experiments of," *International Journal of Plasticity*, vol. 9, pp. 391-40, 1993.
- [21] Y. Jiang and H. Sehitoglu, "Modeling of Cyclic Ratchetting Plasticity, Part I: Development of Constitutive Relations," *Journal of Applied Mechanics*, vol. 63, pp. 720-725, 1996.
- [22] Y. Jiang and H. Sehitoglu, "Modeling of Cyclic Ratchetting Plasticity, Part II: Comparison of Model Simulations With Experiments," *Journal of Applied Mechanics*, vol. 63, pp. 726-733, 1996.
- [23] M. Abdel-Karim and N. Ohno, "Uniaxial Ratchetting of 316FR Steel at Room Temperature Part I: Experiments," *Journal of Engineering Materials and Technology*, 2000.
- [24] M. Abdel-Karim and N. Ohno, "Uniaxial Ratchetting of 316FR Steel at Room Temperature Part II: Constitutive Modeling and Simulation," *Journal of Engineering Materials and Technology*, 2000.
- [25] Perzyna, P., "The thermodynamical theory of elasto-viscoplasticity," *Engineering Transactions*, vol. 53, pp. 235-316, 2005.
- [26] S. Moreau, "Analysis of thermoelastic effects accompanying the deformation of PMMA and PC polymers," *Comptes Rendus Mécaniques*, vol. 333, no. 8, pp. 648-653, 2005.

- [27] T. Hughes and J. Simo, *Computational Inelasticity*, Springer, 2000.
- [28] L. Adam and J. Ponthot, "Thermomechanical modeling of metals at finite strains: First and mixed order finite elements," *International Journal of Solids and Structures*, vol. 42, no. 21, pp. 5615-5655, 2005.
- [29] A. Benaarbia, Y. Rae and W. Sun, "Unified viscoplasticity modelling and its application to fatigue-creep behaviour of gas turbine rotor," *International Journal of Mechanical Sciences*, vol. 136, pp. 36-49, 2018.
- [30] "ITER Organisation web site," [Online]. Available: <https://www.iter.org>.
- [31] R. Budynas and W. Young, *Roark's Formulas for Stress and Strain*, McGraw-Hill, 2002.
- [32] K. Maki, "Nuclear heating in fusion reactor," in *JAERI-Conf-99-002*, Japan, 1999.
- [33] M. Fabbri, "Nuclear heat analysis for the ITER Vacuum Vessel regular sector," *Fusion Engineering and Design*, vol. 137, pp. 435-439, 2018.
- [34] J.-L. Boutard, "Endommagement des alliages métalliques par les neutrons rapides," *Reflets physique*, vol. Numéro 38, pp. 17 - 21, 2014.
- [35] G. Kalinin, "ITER R&D: Vacuum Vessel and In-Vessel components: material development and test," *Fusion Engineering and Design*, vol. 55, pp. 231-246, 2001.
- [36] R. Klueh, "Cladding and Duct Materials for Advanced Nuclear Reactors," *JOM: the journal of the Minerals, Metals & Materials Society*, vol. 60, pp. 15-23, 2008.